Nonlinear Photonic Crystals in $KTiOPO_4$

Mats Nordlöf

ROYAL INSTITUTE
OF TECHNOLOGY

Master of Science Thesis

Laser Physics
Department of Applied Physics
School of Engineering Science
KTH

Stockholm, Sweden 2007

TRITA-FYS: 2007:32
ISSN: 0280-316X
ISRN: KTH/FYS/- -07:32- -SE

Abstract

In this master thesis a method for manufacturing a two-dimensional nonlinear photonic crystal in $KTiOPO_4$ has been presented followed by an analysis of the frequency conversion properties. Two crystals, each of different two-dimensional period, 6.09×6 µm^2 and 6.09×30 µm^2, were realized by a lithographic patterning step and electric field poling. The two-dimensional lattice supports second harmonic generation of a cw laser at different wavelengths, using multiple reciprocal lattice vectors. These results were in very good agreement with a theoretical calculation of the phase-matching properties. The acceptance bandwidth properties has been measured and we found that the bandwidth is up to 3 times larger for non-collinear propagation compared to a one-dimensional collinear interaction. Finally we report on a pulsed duo-line narrowband ($\sim$0.2 nm) coherent light source with tunable wavelength separation ($0-5$ nm) and center wavelength (±1 nm), in the blue spectral region, using a broadband pump.

Sammanfattning

I detta examensarbete har en metod för att tillverka en tvådimensionell ickelinjär fotonisk kristall presenterats och möjligheten för frekvenskonvertering av ljus har undersökts. Två kristaller, var och en med olika tvådimensionell period, 6.09×6 µm^2 och 6.09×30 µm^2, har tillverkats genom en litografisk mönstringsteknik följt av elektrisk fältpolning. Det tvådimensionella gittret genererar frekvensfördubbling av ljus från en kontinuerlig laser vid olika våglängder genom att nyttja multipla reciproka vektorer. Dessa resultat stämde mycket väl med de teoretiska beräkningarna av fasmatchningsvillkoren. Acceptansbandbredden har mätts och vi noterade att bandbredden är upp till 3 gånger större för icke-kolinjär propagering jämfört med det endimensionella kolinjära fallet. Slutligen demonstrerade vi en pulsad smalbandig ($\sim$0.2 nm), tvålinje koherent ljuskälla med avstämbar våglängdsseparation ($0-5$ nm) och centervåglängd (±1 nm) i det blå spektralområdet, pumpad av en bredbandig källa.

Acknowledgements

First of all I would like to thank my supervisor Carlota Canalias for guiding me through this work. I highly appreciate the support you have given me and for always having time for my questions. It has been great to work together with you in the relaxed teamwork environment that signifies the Laserphysics research group. Furthermore, I would also like to express my gratitude to my examiner, Professor Fredrik Laurell, for inviting me to his research group and for offering me such a interesting project. Thanks to Valdas Pasiskevicius for helping me whenever I had problems in my work. Your vast experience in physics and excellent sense of how to do experiments in the lab have helped me a lot! Thanks to my friends Ida and Patrik for tipping me about this thesis project. It has been a pleasure to study with you in Umeå and continuing our master thesis projects here at KTH. Finally, many thanks to all people in this research group for providing such a enjoyable stay, I will miss it!

Contents

1 Introduction

Since the invention of the laser, they have found use in a wide variety of applications. They are found in every day life situations, ranging from your CD and DVD player to barcode scanning in the food store, as well in more specific applications such as material processing, biomedical analysis or range-finding, just to mention a few. These diverse applications demand different properties in terms of wavelength, emitted power, efficiency and package size. The range of accessible wavelengths are limited due to the discrete energy levels in the lasing medium, govern by quantum mechanics. Because of this limitation there is an apparent need for means to access other wavelengths.

If we restrict us to compact, efficient and high beam quality lasers in the spectral range from infrared to ultra violet, there is mainly one candidate of lasers. These are diode-pumped solid state lasers (DPSSL), consisting of a high power laser diode, pumping a medium with a lasing host material. However they are lasing in a number of discrete wavelengths, all around 1 micron, which is a very limited part of the desired spectrum. A way to reach other wavelengths is to make use of a nonlinear frequency conversion process. The basic idea is to generate light at another frequency than that of the original light entering the medium. This can, for example, be achieved in a nonlinear crystal with either second harmonic generation (SHG), sum frequency generation (SFG) or parametric down conversion. Those lasers find applications in many different areas where a efficient, high beam quality and compact lasers are desired, often as a replacement of expensive, bulky and inefficient gas lasers.

Due to dispersion in the material, waves at different wavelength will travel at different velocities and become out of phase, thus reducing the efficiency. Traditionally, birefringent phase-matching (BFM) has been used to obtain the required momentum conservation. BFM suffers from certain inherent limitations while on the other hand the concept of quasi-phase matching (QPM) has proved to have several benefits. In the QPM approach, the interacting waves are brought in phase when they have travel a certain distance and become out of phase. In a ferroelectric crystal, it can be achieved by adding an artificial momentum vector, originating from a periodic modulation of the nonlinear coefficient. This is done by periodically inverting the spontaneous polarization and thus altering the sign of the nonlinearity. This is known as periodic poling (PP) in ferroelectrics, and has been widely used to achieve efficient frequency conversion processes, both in research and in commercial applications, after it was first demonstrated in 1993 [1]. With this technique it is possible to phasematch any conversion in the transparency range of the nonlinear crystal, usually from mid-infrared to near ultra-violet.

However, these one dimensional QPM crystals have some limitations; the

wavelength acceptance bandwidth is relatively small and the tunability is limited. It means that a given QPM crystal will only work for a certain fundamental wavelength with a fixed bandwidth of the generated light. A way to circumvent these limitations is to employ a two-dimensional structure where the sign of the nonlinearity is periodically varying in two dimensions, known as a nonlinear photonic crystal.

1.1 Nonlinear photonic crystals

Photonic crystals will first be described as a logic introduction to nonlinear photonic crystals. Photonic crystals have been a subject of considerable research interest for more than a decade [2]. A photonic crystal consists of a periodic optical structure that is designed to affect the motion of photons, in a similar way that electrons are affected in a semiconductor. This opens up for a wide range of applications such as optical switches, optical transistors and optical diodes, possibly leading to a revolution in information technology. A photonic crystal has a periodic variation of the linear susceptibility $\chi^{(1)}$, which is related to the index of refraction, in one, two or three dimensions. This can be done by combining high refractive index and low refractive index building blocks in a periodic structure, which is usually a challenging experimental task. An important feature is that these structures will exhibit a frequency range of incident light where they are totally reflective. In other words, no light can propagate in this forbidden frequency band gap.

If instead, the second-order susceptibility $\chi^{(2)}$ is periodically modulated and the first order susceptibility $\chi^{(1)}$ is space-independent (constant), it is referred to as a nonlinear photonic crystal (NPC), originally suggested by Berger [3]. Usually this is done by modulating the sign of the second-order susceptibility, where the building blocks are $(+\chi^{(2)})$ and $(-\chi^{(2)})$. Strictly speaking they do not fit the classical definition of a photonic crystal since they do not possess a photonic bandgap [2].

A NPC offers phase matching in two dimensions with the possibility to support several conversion processes simultaneously. This is an important advantage that makes a NPC more versatile compared to a 1D QPM structure. A theoretical work by Lifshitz *et al.* [4] propose a design of a nonlinear photonic quasicrystal that can be utilized for simultaneous phase matching of arbitrary optical frequency-conversion processes.

Another very interesting branch of application arises when nonlinear materials are combined with a photonic crystal. For example, an all optical transistor can be realized by incorporating a nonlinear material in a photonic crystal, theoretically shown by Yanik *et al.* [5]. It works very similar to an electrical transistor; the signal input is not transmitted as long as there is no light present on the control input. But when the control input is present the signal input is transmitted. The combination of the light guiding properties of a photonic crystal and a nonlinear response medium can possibly lead to an all-optical computer. However,

the drawback is that this approach requires high optical powers in order to obtain a nonlinear interaction [6].

1.2 The objective

The objective of this master thesis was to pursue the possibilities to manufacture a second-order nonlinear photonic crystal in the material potassium titanyl phosphate $KTiOPO_4$ (KTP) by means of electric field poling. The work was divided into two parts, where the first aimed to manufacture the NPC by a conventional lithographic step followed by electric field poling and the second part focused on optical characterization of the fabricated structures. The emphasis of the characterization work was to examine the performance offered by a two-dimensional structure, both experimentally and theoretically. Several different experimental setups were used where measurements on phase-matching processes and efficiencies were carried out.

1.3 Outline of the thesis

The work is presented as follows: The second chapter deals with a basic theory of nonlinear optics at a level suitable for describing the experimental part. The main results are the coupled wave equations and the description of second harmonic generation. Chapter three describes the requirement of phase matching in order to achieve an effective frequency conversion process. It also describes concepts from solid state physics that are necessary tools in order to understand the phase-matching process. Chapter four is presenting the nonlinear material KTP used in this work. Both crystal structure and ferroelectric properties as well as the optical properties of the crystal are described. Chapter five is explaining the fabrication method, periodic electric field poling, that was used to realize the structures. Here the results of the optical microscope evaluation of the poled structures are presented. Chapter six is the main chapter describing frequency conversion processes in several different experimental setups. It is divided into two parts; narrowband pumping and broadband pumping, where the first aims to determine the phase-matching processes and the second focuses on simultaneously generation of multiple wavelengths. Following that, the last chapter seven, concludes the work and discusses possible improvements and other continuations.

2 Nonlinear optics

In order to understand the interaction between light and matter, it is necessary to introduce a model that is able to describe the phenomena that are observed. The simplest model is the electron oscillatory model or the Lorentz model of an atom, proposed by H. A. Lorentz [7]. In this model, the electron is assumed to be attached to the atom by a spring. When a dielectric medium is subject to an electromagnetic field, it will induce a displacement of the electron cloud in the material.

Linear optics explains the phenomenon observed when the intensity of the light is sufficiently low. This includes the optical properties that we observe in every day life, for example, the rainbow or the colorful oil films on water. However, after the invention of the laser in 1960, much higher intensities are available. These resulted in completely new possibilities for research in the field of nonlinear optics (NLO). Many interesting properties, due to the nonlinear effects, have been discovered since second harmonic generation was observed for the first time in a quartz crystal.

The nonlinear effects arising in nonlinear material can be understood by using the Lorentz model. A monochromatic oscillating electric field will induce a dipole oscillation at the same frequency as the field. This displacement of the electrons is referred to as the polarization of the dielectric material. The oscillating electric dipole will, in turn, radiate a new electromagnetic field, which is described in standard textbooks on electromagnetic theory, see ref [8].

To a first approximation, the displacement or the polarization is a linear response of the electric field, which explains the linear optical effects. However, with a stronger electric field, the displacement will start to "saturate". This gives a nonlinear response with a distortion of the waveform for the polarization. This distorted polarization can be modeled by higher-order harmonics of the fundamental frequency of the electric field. Hence the radiated electromagnetic field will contain multiples of the fundamental frequency. This is an intuitive way to explain the origin of second- and higher order harmonic generation. The presence of the nonlinear effects does not solely depend on the intensity of the light, but also on the ability of the material itself to generate a nonlinear response. Therefore, it is not possible to give a certain fixed number of the intensity where the nonlinear effects will start to take place.

2.1 Linear optics

In linear optics, the electromagnetic wave induces a separation of the charges in the material, i.e., a polarization, which is directly proportional to the electric field. In crystals, the polarization induced by an electric field and the field itself are not necessarily parallel. Therefore, the relation between the linear electric polarization and the electric field is given by a tensor relation:

$$\mathbf{P}_L = \varepsilon_0 \boldsymbol{\chi}^{(1)} \mathbf{E} \ , \tag{2.1}$$

where the subscript L refers to the linear polarization, ε_0 is the permittivity of vacuum, and $\boldsymbol{\chi}^{(1)}$ is the linear dielectric response tensor, or susceptibility. This relation can also be written as a sum of the scalar elements of the tensor,

$$P_{L,i} = \varepsilon_0 \sum_j \chi_{ij}^{(1)} E_j \ , \tag{2.2}$$

where the indices ij signify the cartesian coordinates, $(i, j) = (x, y, z)$. It can be shown that the susceptibility tensor is symmetric and, therefore, it can be diagonalized [9]. This means that the electric field and the induced polarization can be oriented in a coordinate system such that the susceptibility tensor has only diagonal, nonzero elements:

$$\boldsymbol{\chi}^{(1)} = \begin{pmatrix} \chi_{11}^{(1)} & 0 & 0 \\ 0 & \chi_{22}^{(1)} & 0 \\ 0 & 0 & \chi_{33}^{(1)} \end{pmatrix} \ . \tag{2.3}$$

The components χ_{ii} are related to the index of refraction according to,

$$n_i = \sqrt{1 + \chi_{ii}^{(1)}} \ . \tag{2.4}$$

This is the physical description of birefringence; light polarized in different directions will experience different indices of refraction.

2.2 The constitutive relations

When the intensity of the light is sufficiently large, the material will have a nonlinear response and then it is necessary to modify the above relation between the electrical field and the electric polarization. One way to describe this is to make a series expansion in the applied field,

$$\mathbf{P} = \varepsilon_0 \boldsymbol{\chi}^{(1)} \mathbf{E} + \varepsilon_0 (\boldsymbol{\chi}^{(2)} \mathbf{E}^2 + \boldsymbol{\chi}^{(3)} \mathbf{E}^3 + \dots) = \mathbf{P}^L + \mathbf{P}^{NL} \ , \tag{2.5}$$

where $\mathbf{P}^L$ is the linear part of the polarization and $\mathbf{P}^{NL}$, correspondingly, is the nonlinear part, ε_0 is the permittivity of vacuum, and $\boldsymbol{\chi}^{(m)}$ is the susceptibility tensor of m:th order and rank $(m + 1)$. It is important to note that the field

in Eq. (2.5) is the total applied field, which can be a superposition of many different frequencies. From now on, the treatment presented here will only deal with second-order nonlinear processes, known as $\chi^{(2)}$-processes.

A suitable way to analyze the problem is to write the Fourier components of the nonlinear polarization. Assume that there are only two electric fields present oscillating at frequencies ω_1 and ω_2 and the 2:nd order polarization oscillating at ω_3. This will give the following frequencies for the 2:nd order polarization: $2\omega_1$, $2\omega_2$, $\omega_1 + \omega_2$, $\omega_1 - \omega_2$ and a DC term at zero frequency, a mathematical result of the squared electric field. To pursue the symmetry properties of the susceptibility tensor, it is common to write the i:th cartesian component of the complex polarization as follows,

$$P_i^{(2)}(\omega_3) = \varepsilon_0 D^{(2)} \sum_{jk} \chi_{ijk}^{(2)}(-\omega_3; \omega_1, \omega_2) E_j(\omega_1) E_k(\omega_2) \ . \tag{2.6}$$

The sum will run over the cartesian coordinates, namely $(j, k) = (x, y, z)$. And the degeneracy factor is given by,

$$D^{(2)} = \begin{cases} 1 & \text{for indistinguishable fields} \\ 2 & \text{for distinguishable fields} \end{cases} \ . \tag{2.7}$$

All fields are distinguishable except when the two fields have the same frequency and traveling in the same direction. The second-order polarization, $P^{(2)}$, is oscillating at the frequency ω_3, given by the energy conservation $\omega_3 = \omega_1 + \omega_2$ which gives rise to a set of different processes.

When two photons at different frequencies, ω_1 and ω_2, travel through the nonlinear medium they can either add or subtract in frequency and hence create a new photon at either higher or lower energy. Sum-frequency generation (SFG) is defined as the case when they add in frequency, $\omega_3 = \omega_1 + \omega_2$, and difference-frequency generation (DFG) is defined as when they subtract in frequency, $\omega_3 = \omega_1 - \omega_2$. Second harmonic generation (SHG) is a special case of the nonlinear frequency mixing where the two input photons have the same frequency, $\omega_1 = \omega_2 = \omega$, and the generated photon will thus have twice the frequency, $\omega_3 = 2\omega$. See figure (2.1) for a schematic description. In this master thesis, only the case of 2:nd order nonlinear interaction, i.e. second harmonic generation will be studied.

The first symmetry aspect derived from Eq. (2.6) is that there is no physical difference between interchanging the order of the product of the fields, $E_j(\omega_1)E_k(\omega_2)$. Therefore it is possible to write the nonlinear susceptibility in a contracted form according to the following subscript transformation:

i;	x	1	jk;	xx	l;	1
	y	2		yy		2
	z	3		zz		3
				$yz = zy$		4
				$xz = zx$		5
				$xy = yx$		6

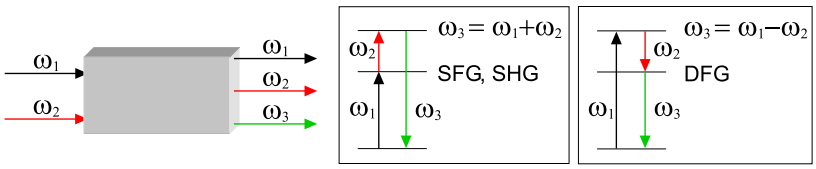

Figure 2.1. *Schematic description of the interactions in second-order nonlinear processes.*

This is called the intrinsic permutation symmetry and the result is that the nonlinear coefficient is reduced from a $3\times3\times3$ tensor to a 3×6 tensor. When dealing with second-order nonlinearities it is common to introduce the **d**-tensor, with contracted elements according to, $d_{il} = \frac{1}{2}\chi^{(2)}_{ijk}$. The tensor can be further contracted if the Kleinman symmetry holds [10]. It requires two conditions to be fulfilled. Firstly, the material is assumed to be essentially lossless (i.e., the interacting frequencies are far from the material resonances) and, hence, the susceptibility is a real entity. Secondly, the material is assumed to have no absorption lines between the interacting frequencies. Imposing these symmetries will reduce the **d**-tensor to 10 unique elements weakly depending on the frequency [11]. However, in the literature, the **d**-tensor is usually written with its 18 elements in the following equation:

$$\begin{pmatrix} P_x^{(2)}(\omega_3) \\ P_y^{(2)}(\omega_3) \\ P_z^{(2)}(\omega_3) \end{pmatrix} = 2\varepsilon_0 D^{(2)} \begin{pmatrix} d_{11} & d_{12} & d_{13} & d_{14} & d_{15} & d_{16} \\ d_{21} & d_{22} & d_{23} & d_{24} & d_{25} & d_{26} \\ d_{31} & d_{32} & d_{33} & d_{34} & d_{35} & d_{36} \end{pmatrix} \times \begin{pmatrix} E_x(\omega_1)E_x(\omega_2) \\ E_y(\omega_1)E_y(\omega_2) \\ E_z(\omega_1)E_z(\omega_2) \\ E_y(\omega_1)E_z(\omega_2) + E_z(\omega_1)E_y(\omega_2) \\ E_x(\omega_1)E_z(\omega_2) + E_z(\omega_1)E_x(\omega_2) \\ E_x(\omega_1)E_y(\omega_2) + E_y(\omega_1)E_x(\omega_2) \end{pmatrix}, \tag{2.8}$$

where $D^{(2)}$ is the same as in Eq. (2.7).

Only noncentrosymmetric crystals will exhibit even order of nonzero susceptibility. A centrosymmetric crystal can be understood by considering an electron's motion. It will experience a symmetric (with respect to the electron displacement) potential well whereas in the noncentrosymmetric crystal, the potential well is not symmetric. Depending on the symmetry of the crystal class, the number of nonzero elements in the nonlinear tensor can be less than the 18 independent ones in Eq. (2.8). For a given physical geometry, it is possible to reduce the vectorial form of Eq. (2.8) to a scalar relation via the effective d-coefficient, d_{eff}. It is calculated as a weighted average of the different components depending on the direction of propagation and the polarization of the electric field relative to the crystallographic axes:

$$P^{(2)}(\omega_3) = \varepsilon_0 D^{(2)} d_{eff} E(\omega_1) E(\omega_2) \ . \tag{2.9}$$

This contracted notation will be used in the following sections.

2.3 The coupled wave equations

Maxwells equations are the fundamental description of electric and magnetic fields interacting with a medium. Eliminating the magnetic fields in Maxwells equations lead to the wave equation for the transverse electric field. In the following derivation, it is assumed that the fields are monochromatic infinite plane waves. In the case of a loss-less, neutral dielectric medium (one with no free charges) and with a low magnetic permeability, Maxwells equation can be written as:

$$\nabla^2 \mathbf{E} = \mu_0 \varepsilon_0 \frac{\partial^2 \mathbf{E}}{\partial t^2} + \mu_0 \frac{\partial^2 \mathbf{P}}{\partial t^2} \ , \tag{2.10}$$

where μ_0 is the permeability of vacuum. This equation governs the evolution of the electric field due to the driving polarization. The polarization term in Eq. (2.10) is the total polarization consisting of a linear and a nonlinear term according to the right hand side of Eq. (2.5).

Let the total field be a set of monochromatic plane waves propagating along the x-direction,

$$\begin{aligned} \mathbf{E}(x,t) &= \frac{1}{2} \sum_n \left[\mathbf{E}_n(x) \exp(i(k_n x - \omega_n t)) + c.c. \right] \ , \\ \mathbf{P}(x,t) &= \frac{1}{2} \sum_n \left[\mathbf{P}_n(x) \exp(i(k'_n x - \omega_n t)) + c.c. \right] \ , \end{aligned} \tag{2.11}$$

where the sums extend over all positive frequencies. The specific frequency component is denoted ω_n with the corresponding wave vector, $k_n = \frac{\omega_n n(\omega_n)}{c}$, where $n(\omega_n)$ is the index of refraction. The envelopes of the propagating waves are given by $\mathbf{E}_n$ and $\mathbf{P}_n$, respectively.

Substituting the frequency components into Eq. (2.10) yields:

$$\frac{\partial^2 \mathbf{E}(x,t)}{\partial x^2} + \mu_0 \varepsilon_0 \omega_n^2 (1 + \boldsymbol{\chi}^{(1)}) \cdot \mathbf{E}(x,t) = -\mu_0 \omega_n^2 \mathbf{P}^{(NL)}(x,t) \ . \tag{2.12}$$

It can be seen that the polarization has been split into its linear and nonlinear parts where the linear part defines the dielectric tensor, $\boldsymbol{\epsilon} = 1 + \boldsymbol{\chi}^{(1)}$. And the index of refraction is given by the real part, $\mathbf{n} = \mathrm{Re}\sqrt{1 + \boldsymbol{\chi}^{(1)}}$. This index is in general a tensor, but, in the case of a isotropic medium, it reduces to a scalar. In the case of a nonisotropic crystal, it gives rise to birefringence.

The envelope of the wave, $\mathbf{E}_n$, varies when propagating through the medium. If we assume that this variation is slow, both in amplitude and in phase, over distances of the order of the wavelength, then:

$$\left| \frac{\partial^2 \mathbf{E}_n}{\partial x^2} \right| \ll \left| k_n \frac{\partial \mathbf{E}_n}{\partial x} \right| \ . \tag{2.13}$$

This is known as the slowly varying envelope approximation (SVEA) and is almost always valid in nonlinear processes. By invoking this approximation on Eq. (2.12), using the frequency components of the fields shown in Eq. (2.11) the wave-equation will now reduce to a first-order differential equation:

$$\frac{\partial \mathbf{E}_n}{\partial x} = \frac{i \mu_0 \omega_n^2}{2 k_n} \mathbf{P}_n^{NL} \exp(-i k_n x) \ . \tag{2.14}$$

Here, the relation $k_n^2 = \omega_n^2 \mu_0 \epsilon_0 (1 + \chi^{(1)})$ has been used. This equation describes the evolution of the electric field due to the nonlinear polarization as a source term in a general, nonlinear optical process.

For the case of a second-order, nonlinear interaction, there are three different interacting fields and hence, three equations describing the system. These are obtained by using the d_{eff} description of Eq. (2.9) together with the wave-equation, Eq. (2.14), and we obtain the following:

$$\begin{aligned}
\frac{\partial E_1}{\partial x} &= \frac{i\omega_1}{n_1 c_0} d_{eff} D^{(2)} E_3 E_2^* \exp(i \Delta k x) \ , \\
\frac{\partial E_2}{\partial x} &= \frac{i\omega_2}{n_2 c_0} d_{eff} D^{(2)} E_3 E_1^* \exp(i \Delta k x) \ , \\
\frac{\partial E_3}{\partial x} &= \frac{i\omega_3}{n_3 c_0} d_{eff} D^{(2)} E_1 E_2 \exp(-i \Delta k x) \ ,
\end{aligned} \tag{2.15}$$

where the degeneracy factor, $D^{(2)}$, is given in Eq. (2.7). The energy conservation is then given by the relation $\omega_3 = \omega_1 + \omega_2$ and $\Delta k = k_3 - k_2 - k_1$ is the phasemismatch between the interacting waves. This set of equations is known as the coupled-wave equations which is the natural starting point in the analysis of second-order nonlinear processes.

2.4 Second harmonic generation

First demonstrated in 1961, second harmonic generation is the most simple nonlinear process. It is often convenient to look at this process in the photon picture. Two identical incoming photons at frequency ω are added in the nonlinear material and will create one outgoing photon at twice the frequency, $\omega_{SH} = 2\omega$. The coupled-wave equations, Eq. (2.15), will then describe the evolution of the generated field, $E_{2\omega} = E_3$. In most cases, one can assume that the pump beam is not depleted during the propagation through the crystal. In a mathematical description, this would read, $E_1(0) = E_1(L)$ and $E_2(0) = E_2(L)$, where L is the interaction length of the nonlinear crystal. This can be motivated by the fact that the intensity of the generated beam is much smaller than the pump beam. The material is also assumed to be essentially lossless in the range of the interacting frequencies. Integrating the last equation in Eq. (2.15) over the crystal length L and using the definition of the field intensity, $I_i = \frac{1}{2}\varepsilon_0 c_0 n_i |E_i|^2$, yields,

$$I_{2\omega} = \frac{2\omega^2 d_{eff}^2 L^2 I_\omega^2}{n_\omega^2 n_{2\omega} c_0^3 \varepsilon_0} \mathrm{sinc}^2\left(\frac{\Delta k L}{2}\right) , \tag{2.16}$$

$$\Delta k = k_{2\omega} - 2k_\omega \ . \tag{2.17}$$

The subscripts ω and 2ω refer to the fundamental and the second harmonic beams, respectively. The sinc-function is defined as $\mathrm{sinc(x)} = \sin(x)/x$ and Δk is the phasemismatch expressed in wave vectors for the fundamental and the second harmonic beams, respectively. As a consequence, the efficiency is proportional to L^2 and the fundamental intensity squared, I_ω^2. In figure 2.2 the sinc^2-function is plotted. It can be seen that the intensity will drastically decrease when $\Delta k L \neq 0$, with minima at $\Delta k L = 2\pi m$, $(m = \pm 1, \pm 2, ...)$.

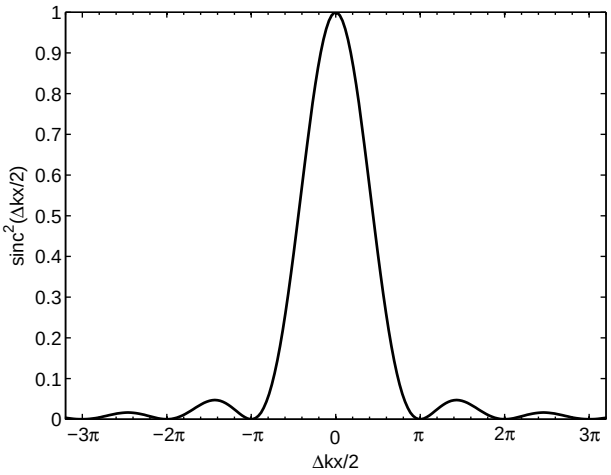

Figure 2.2. *Plot of the sinc^2-function as a function of phasemismatch*

The intensity of SH generation does also depend on the nonlinear material. This is often summarized in a parameter known as *the figure of merit*, $d_{eff}^2/(n_\omega^2 n_{2\omega})$, which depends on the d-coefficient and the indices of refraction.

In general, the fundamental and the second harmonic waves will travel at different phase velocities due to dispersion in the medium. The phase difference, Δk, will therefore oscillate during the propagation through the medium and therefore, it is impossible to generate any considerable amounts of second harmonic intensity. There are several different ways to achieve phase matching and they will be discussed in the next chapter.

3 Phase-matching techniques

A nonlinear frequency conversion process is in general not efficient unless both the energy conservation and momentum conservation are fulfilled. Figure 3.1 illustrates the intensities of the fundamental and second harmonic waves as well as the intensity curve for perfect phase matching, ($\Delta k = 0$). Due to dispersion the interacting waves will become out of phase after a certain distance defined as the coherence length, $L_c = \pi/|\Delta k|$, (not to be confused with the statistical coherence of light). After one coherence length the intensity of the second harmonic field will start to convert back to the fundamental field, a process known as back conversion. However, if the interacting waves can be kept in phase, the intensity will grow quadratically with the interaction length L (dotted curve and upper horizontal scale). The factor $G^2 = \frac{2\omega^2 d_{eff}^2}{\varepsilon_0 c_0^3 n_\omega^2 n_{2\omega}} I_\omega(0)$, is introduced to make it possible to plot Eq. (2.17). The results are only true in the regime where the pump is negligibly depleted, for the more extensive analysis of pump depletion, see [11].

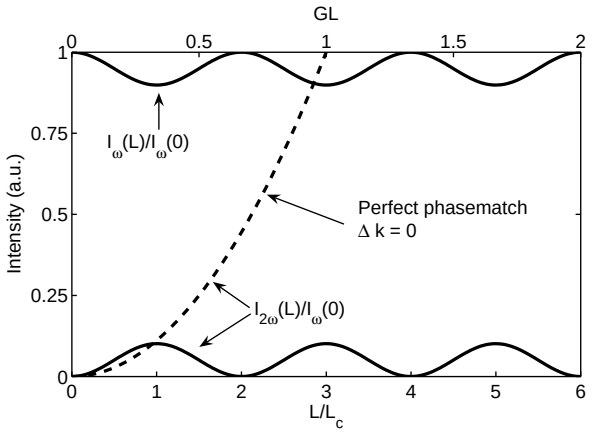

Figure 3.1. *Plot of intensity dependence for perfect phasematch (dotted curve and upper horizontal scale), and finite phasematch (continuous curves and lower horizontal scale).*

To summarize, the goal is to minimize the phase mismatch between the interacting waves. A few different methods will be shortly reviewed with main focus on the concept of quasi-phase matching, which has been employed in this thesis.

3.1 Birefringent phase-matching

A popular way to achieve phase matching is to take advantage of the birefringency of a crystal. Birefringence means that the index of refraction will depend upon the polarization of the incoming wave. Consider Eq. (2.17) rewritten in terms of index of refraction,

$$\Delta k = \frac{2\omega}{c_0}(n_{2\omega} - n_\omega) \ . \tag{3.1}$$

It is evident that the waves will be in phase whenever $n_\omega = n_{2\omega}$. This can be achieved by letting the incoming wave have a polarization different of the generated wave. For a certain geometry of the crystal relative to the propagating waves, they will possibly experience the same index of refraction.

One should note that it is not always easy to fulfill all the requirements for a given frequency conversion process. First of all the material has to be transparent in range of the frequencies used. Furthermore the birefringence has to be large enough to satisfy the phase-matching requirements. As a consequence of material choice and geometry of propagation, the nonlinear coefficient attainable is usually not the largest available. In most of the cases the fundamental beam cannot be aligned along a principal axis of the crystal because of the phase-matching condition, and hence the fundamental and second harmonic waves will quickly diverge from each other. This is known as spatial walk-off which will greatly limit the effective interaction length. However, the greatest advantage of birefringent phase matching is the simplicity of the method. It is possible to grow large crystals of good quality without any post-processing steps after the growth.

3.2 Quasi-phase matching

The idea of quasi-phase matching was suggested already in 1962 by Armstrong *et al.* [12], shortly after the first experiment on second harmonic generation. However it was not until three decades later the technique proved to be useful. The concept is to introduce a periodic modulation in the material that will reset the phasemismatch after each coherence length. The first experiments utilizing QPM was based on a stack of thin quartz plates rotated 180 degrees relative to the one before, each of thickness of many coherence lengths. By doing so the sign of the second order nonlinear coefficient is altered and thereby resulting in a reset of the phase. A major problem was the reflection losses at each layer boundary. As we will see there are other ways to approach the problem that have been proven to be more convenient.

Ideally, the modulation is done after each coherence length, L_c, and is then referred to as first order QPM, see figure 3.2. One can also use higher order QPM where the material is modulated with a period of several coherence lengths. The drawback is that the efficiency is reduced for higher orders.

A theoretical description of QPM has been provided by Fejer *et al.* [13]. To understand the generalization to two-dimensional phase matching it is necessary

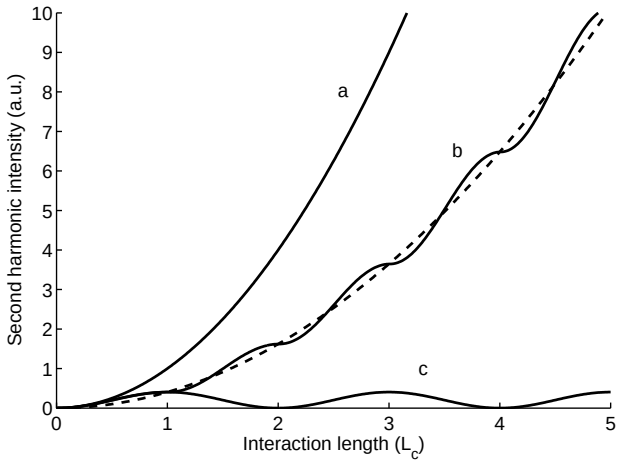

Figure 3.2. *Second harmonic generation in a material with different phase-matching conditions. Line (a): Perfect phase matching. Line (b): First order QPM where the sign of the nonlinearity is flipped every coherence length. Line (c): Finite phase matching. The dotted curve is the perfect phase-matching curve reduced by a factor* $(2/\pi)^2$ *for first order QPM.*

to start with a mathematical framework for the one-dimensional case. Consider the nonlinear coefficient varying with position, $d = d(z)$. The results of the coupled wave equations are not valid since d_{eff} is no longer constant along the crystal. In most cases the modulation is done such that the sign of the nonlinear coefficient is altered every coherence length. The normalized form of $d(z)$ can then be written,

$$g(z) = d(z)/d_{eff} \ , \tag{3.2}$$

with range $-1 < g(z) < 1$. Since $g(z)$, is a periodic function of period $\Lambda \equiv 2L_c$ it can be expressed as a Fourier series,

$$g(z) = \sum_{m=-\infty}^{\infty} G_m \exp\left(iK_m z\right) \ , \tag{3.3}$$

with, so called, m:th-harmonic grating vector,

$$K_m = \frac{2\pi m}{\Lambda} \ . \tag{3.4}$$

Assuming SHG again and integrating the last equation in Eq. (2.15) over the crystal length and replacing d_{eff} by the spatially varying $d(z)$ in Eq. (3.2)-(3.3) yields,

$$E_{2\omega} = \frac{i\omega E_\omega^2 d_{eff}}{n_{2\omega} c_0} \int_0^L \sum_{m=-\infty}^{\infty} G_m \exp\left(i\left(K_m - k_{2\omega} + 2k_\omega\right) z\right) dz \ , \tag{3.5}$$

where $\Delta k' = k_{2\omega} - 2k_{\omega}$. The main contribution to this integral will be for $K_m - \Delta k' \approx 0$, since all other terms are oscillating harmonics that vanish in the integration. The new nonlinear coefficient will be reduced by the Fourier coefficient according to, $d_{QPM} = G_m d_{eff}$. These coefficients will depend on the periodic function $g(z)$. The most common QPM structures are those where the sign of $g(z)$ switches between -1 and 1 with a period of Λ. The duty cycle is defined as, $D = l/L$, where l is the length of the sections with positive sign. Figure 3.3 shows a crystal of 50 % duty-cycle.

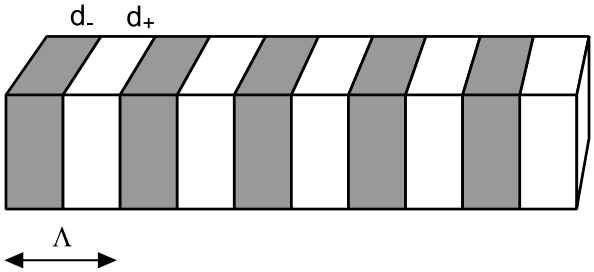

Figure 3.3. *Illustration of a 1D QPM crystal where the d-coefficient is periodically switched between positive and negative value.*

The Fourier coefficients for this rectangular function, $g(z)$, is given by a standard transform pair,

$$G_m = \frac{2}{m\pi} \sin(m\pi D) \ . \tag{3.6}$$

Hence, the most efficient phase matching will be for first order QPM ($m = \pm 1$) and duty-cycle of 50 % ($D = 1/2$). In this configuration the effective nonlinear coefficient for the intensity (squared electric field) will be reduced by a factor $(2/\pi)^2$, as expected from figure 3.2. Note that only odd orders of QPM will be present for a duty-cycle of 50 %.

Typically the coherence length is in the order of a few microns, depending on the nonlinear process and the material present. That is mainly the reason why it took so long time until QPM proved to be a useful technique; it was not possible to produce a material with such a short period. Another requirement for efficient frequency conversion is that the modulation is done consistently over a distance of several millimeters.

A disadvantage of QPM is the extra processing steps related to the manufacturing, compared to BFM. However, while implementing phase matching in multiple directions in two-dimensional nonlinear crystals, QPM is the sole option. The theoretical derivation of two-dimensional QPM is presented in next section.

3.3 Two-dimensional quasi-phase matching

A natural generalization of the one-dimensional QPM scheme is to extend the phase-matching possibilities to two or three dimensions. This thesis will only deal with two-dimensional QPM for SHG in nonlinear crystals. One usually refers to $\chi^{(2)}$ photonic crystals for engineered structures in which the second order nonlinearity varies periodically. The first to propose a NPC was Berger, [3], and his theoretical work will be the basis for the analysis presented here. The essential features of the two-dimensional theoretical description is very similar to QPM in one dimension, presented in the previous section.

Figure 3.4 shows an example of a nonlinear photonic crystal where the second-order nonlinearity switches periodically between positive and negative value, with a translation symmetry in the 2D lattice.

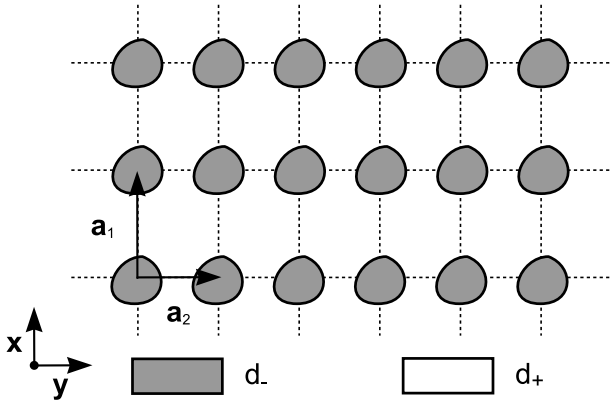

Figure 3.4. *Schematic picture of a 2D $\chi^{(2)}$ crystal. It shows a rectangular lattice with translation invariance perpendicular to the figure. The unit cell is defined by the primitive vectors $\mathbf{a}_1$ and $\mathbf{a}_2$.*

3.3.1 Reciprocal lattice

The concept of reciprocal lattice (RL) is introduced since it will greatly simplify the theoretical description of nonlinear photonic crystals. The similarity with models developed in solid state physics is striking. In the frame of a $\chi^{(2)}$ crystal, the lattice will be built up by a periodic array of positive and negative valued d-coefficients. Whereas in solids the lattice consist of atoms or molecules arranged in a periodic structure.

It is known that a set of periodic layers of atoms in a solid will scatter x-rays according to the Bragg law. This happens due to interference between the different scattered rays. It can be used to gain information about the crystalline structure of the material. Unfortunately the pattern of diffracted beams is not a direct image of the crystal structure. The most common way to explain diffraction

experiments is to link the real crystalline structure, or real lattice to the reciprocal lattice.

It is constructed from the real lattice according to a explicit relation. Let $\mathbf{a}_1$, $\mathbf{a}_2$ and $\mathbf{a}_3$ be primitive vectors of the real lattice. Then the reciprocal lattice is generated by the following primitive vectors,

$$\begin{aligned} \mathbf{b}_1 &= 2\pi \frac{\mathbf{a}_2 \times \mathbf{a}_3}{\mathbf{a}_1 \cdot (\mathbf{a}_2 \times \mathbf{a}_3)} \ , \\ \mathbf{b}_2 &= 2\pi \frac{\mathbf{a}_3 \times \mathbf{a}_1}{\mathbf{a}_1 \cdot (\mathbf{a}_2 \times \mathbf{a}_3)} \ , \\ \mathbf{b}_3 &= 2\pi \frac{\mathbf{a}_1 \times \mathbf{a}_2}{\mathbf{a}_1 \cdot (\mathbf{a}_2 \times \mathbf{a}_3)} \ . \end{aligned} \tag{3.7}$$

In this thesis only the rectangular two-dimensional lattice will be discussed, which have a simple relation between the real and reciprocal lattice. Let the primitive vectors be orientated along a cartesian coordinate system, $\mathbf{a}_1 = a_1\hat{\mathbf{x}}$ and $\mathbf{a}_2 = a_2\hat{\mathbf{y}}$. Then the reciprocal lattice vectors are given by,

$$\begin{aligned} \mathbf{b}_1 &= \frac{2\pi}{a_1}\hat{\mathbf{x}} \ , \\ \mathbf{b}_2 &= \frac{2\pi}{a_2}\hat{\mathbf{y}} \ . \end{aligned} \tag{3.8}$$

Figure 3.4 and 3.5 show the real and reciprocal lattices, respectively, of a rectangular lattice. Note how the longer primitive vector in the real lattice becomes the shorter in the reciprocal lattice.

3.3.2 The coupled wave equations in 2D

The electric field and polarization field is again assumed to be a superposition of monochromatic waves,

$$\begin{aligned} \mathbf{E}(\mathbf{r},t) &= \frac{1}{2}\sum_n \left[\mathbf{E}_n(\mathbf{r})\exp(i(\mathbf{k}_n \cdot \mathbf{r} - \omega_n t)) + c.c.\right] \ , \\ \mathbf{P}(\mathbf{r},t) &= \frac{1}{2}\sum_n \left[\mathbf{P}_n(\mathbf{r})\exp(i(\mathbf{k}_n^{'} \cdot \mathbf{r} - \omega_n t)) + c.c.\right] \ , \end{aligned} \tag{3.9}$$

where $\mathbf{r} = (x, y)$ is the 2D spatial coordinate. As previous, $\mathbf{E}_n$ and $\mathbf{P}_n$ are the wave envelopes and subscript n refer to a individual frequency component. The vectorial form of the SVEA reads,

$$\left|\nabla^2 \mathbf{E}_n(\mathbf{r})\right| \ll \left|\mathbf{k}_n \cdot \nabla\left[\mathbf{E}_n(\mathbf{r})\right]\right| \ . \tag{3.10}$$

By invoking this approximation and using the frequency components of Eq. (3.9) in the wave equation, Eq. (2.12), yields the vectorial wave equation for frequency component n,

$$\nabla \left[\mathbf{E}_n(\mathbf{r})\right] = \frac{i\mu_0\omega_n^2}{2k_n}\mathbf{P}_n^{NL}\exp(-i\mathbf{k}_n\cdot\mathbf{r}) \ . \tag{3.11}$$

Again, it is convenient to use the d_{eff} description similar to Eq. (2.9). And since the evolution of the second harmonic field is of main interest, only the last equation of the coupled wave equations, Eq (2.15), will be considered.

$$\nabla \left[E_{2\omega}(\mathbf{r})\right] = \frac{i\omega E_\omega^2}{n_{2\omega}c_0}d_{eff}(\mathbf{r})\exp(-i\Delta\mathbf{k}\cdot\mathbf{r}) \ , \tag{3.12}$$

where $\Delta\mathbf{k} = \mathbf{k}_{2\omega} - 2\mathbf{k}_\omega$ is the phasemismatch between the second harmonic and fundamental waves. The explicit spatial dependence of d_{eff} is written to stress that a periodic modulation in the medium is already assumed.

Similarly to the 1D QPM method, the second order nonlinearity is periodically modulated, but now in two dimensions. As before, the sign of the d-coefficient switches between positive and negative value and the first order susceptibility (index of refraction) is constant. A convenient way to describe this 2D mesh of modulation is to transform the real lattice to the reciprocal lattice. The lattice points, involved in the phase matching are specified by a reciprocal lattice vector (RLV) $\mathbf{K}$. This enables us to write the normalized form of $d(\mathbf{r})$ as a Fourier series,

$$g(\mathbf{r}) = \sum_{\mathbf{K}\in\mathrm{RL}} G_{\mathbf{K}}\exp(i\mathbf{K}\cdot\mathbf{r}) \ , \tag{3.13}$$

where the sum is extended over the whole 2D reciprocal lattice. Similarly to the ordinary QPM, we integrate the right hand side (RHS) of Eq. (2.14) over the crystal area and replace d_{eff} with the spatially periodic Fourier series in Eq. (3.13). The left hand side (LHS) is evaluated via a line integral along a path that bounds the area A in the real lattice. The interesting result is that the LHS of Eq. (3.13) is proportional to $E_{2\omega}$, for more information, see [14].

$$\mathrm{RHS} = \frac{i\omega E_\omega^2}{n_{2\omega}c_0}\int_A \sum_{\mathbf{K}\in\mathrm{RL}} G_{\mathbf{K}}\exp\left(i\left(\mathbf{K} - \mathbf{k}_{2\omega} + 2\mathbf{k}_\omega\right)\cdot\mathbf{r}\right)\mathrm{d}r \ . \tag{3.14}$$

The growth of the second harmonic field will be maximized when the exponent is zero, with the same arguments following Eq. (3.5). Hence the phase-matching condition in 2D QPM reads,

$$\mathbf{K} - \mathbf{k}^{2\omega} + 2\mathbf{k}^{\omega} = \mathbf{0} \ . \tag{3.15}$$

In this thesis, the RLV $\mathbf{K}_{mn}$ is labeled by two subscripts, m and n, specifying the incremental step in x- and y-directions, respectively. Figure 3.5 shows the reciprocal lattice for two different phase-matching processes. Two angles are introduced to describe the geometrical configuration. The internal spatial walk-off angle is denoted 2θ and the internal incidence angle of the fundamental beam is ϕ_{int}. The lattice is arranged such that the x- and y-axis is aligned with the crystallographic a- and b-direction, respectively. Therefore the left part of the figure illustrates normal incidence. One should note that the intensity of SHG becomes weaker for increasing index n, or equivalently increasing angle θ. This is due to the shorter effective interaction length which is given by the length i x-direction where the fundamental and SH beams overlap. Efficient frequency conversion will only take place where the beams physically overlap. The interaction length will not only depend on the angle θ but also on the beam waists and, hence, the focusing condition.

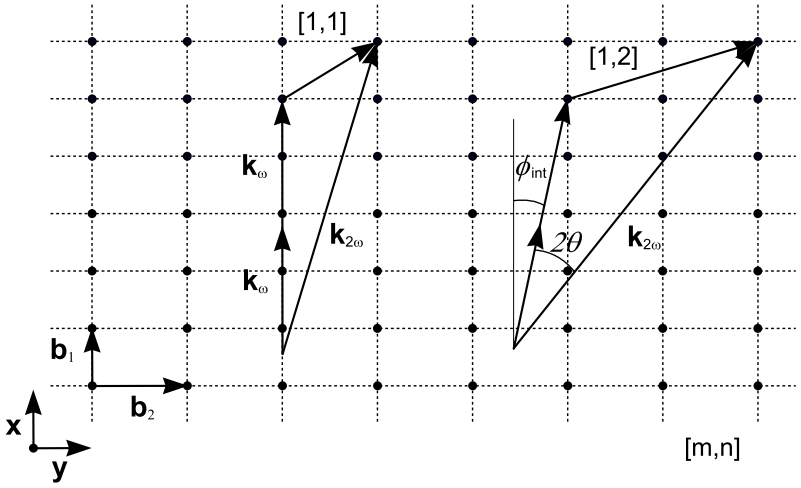

Figure 3.5. *Reciprocal lattice of a rectangular structure with the 2D QPM processes of order [1,1] and [1,2] shown schematically. 2θ is the internal walk-off angle and ϕ_{int} is the internal incidence angle of the fundamental beam.*

Using some geometry one can relate the the SH wavelength to the walk off angle for the case of normal incidence,

$$\frac{\lambda_{2\omega}}{n_{2\omega}} = \frac{2\pi}{|\mathbf{K}_{mn}|}\sqrt{\left(1-\frac{n_\omega}{n_{2\omega}}\right)^2 + 4\frac{n_\omega}{n_{2\omega}}\sin^2\theta}\ , \tag{3.16}$$

where $\lambda_{2\omega}$ is the SH vacuum wavelength and $\mathbf{K}_{mn}$ is the RLV used. As usual, the indices of refraction n_ω and $n_{2\omega}$ refer to the fundamental and SH beam, respectively. This equation gives the direction of radiation at wavelength 2λ and can be seen as the *nonlinear Bragg law*. If the medium has no dispersion,

$n_\omega = n_{2\omega}$, Eq. (3.16) is reduced to the well known Bragg law,

$$\lambda = \frac{4\pi}{|\mathbf{K}|} \sin\theta = 2d \sin\theta \ , \tag{3.17}$$

where d is the distance between atomic layers.

The nonlinear Bragg law does not give any information about the intensity of the generated SH radiation. It suggests that a continuum of angles should exist for a continuous range of wavelengths. This is of course not the case since the QPM condition ($\Delta k = 0$) should be fulfilled. Therefore some directions will be phasematched while others not. The way to picture the QPM condition in 2D is the Ewald construction

3.3.3 Ewald construction

With the concept of the reciprocal lattice it is possible to easily analyze the geometry of the diffracted beams thanks to the Ewald construction. That is a simple geometrical construction used in x-ray experiments for interpreting diffraction patterns. The modified Ewald construction used in 2D QPM was suggested by Berger [3], and follows the same principle as the usual Ewald construction. More information on the Ewald construction used in crystallography can be found in a standard book in solid state physics, see Ashcroft [15] for example.

Consider a two-dimensional crystal with its corresponding reciprocal lattice. Given the incident wave vector $\mathbf{k}_\omega$, draw an arrow along the direction of propagation ending at the origo, O_{RL}, of the reciprocal lattice with length $|2\mathbf{k}_\omega|$. Then draw a circle of radius $|\mathbf{k}_{2\omega}|$ with its center located where the $2\mathbf{k}_\omega$ vector begins. This is the Ewald "sphere" (in the 2D case a circle). If the circle intersects a lattice point there will be a SH peak generated with corresponding RLV $\mathbf{K}_{mn}$. In figure 3.6 the $[1, 1]$ SH peak is shown. It can be seen from the figure that two peaks will always be generated simultaneously if the pump beam impinges under normal incidence.

As in the case of x-ray diffraction, there will be no phase matching for a general incident pump beam. Generation of SH peaks can be obtained by either varying the wavelength or the angle of propagation of the pump. Both of these alternatives are thourougly examined in the experimental part of this thesis.

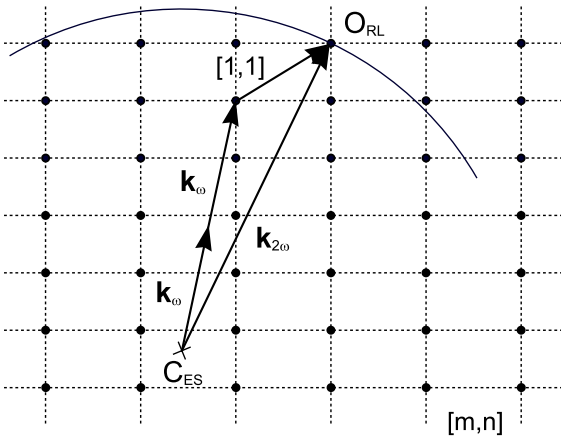

Figure 3.6. *Nonlinear Ewald construction. SH beams will be generated wherever the Ewald sphere intersects a lattice point.*

When the sample is rotated and the wavelength is kept fixed, it is possible to write an analytical expression equivalent to the Ewald construction. It is simply a projection of the vector components in x- and y-directions. The system of equations that has to be fulfilled for SH generation is given by,

$$\begin{cases} \mathbf{k}_{2\omega}\cos(2\theta+\phi_{int}) - 2\mathbf{k}_{\omega}\cos\phi_{int} = mK_x \\ \mathbf{k}_{2\omega}\sin(2\theta+\phi_{int}) - 2\mathbf{k}_{\omega}\sin\phi_{int} = nK_y \end{cases}, \tag{3.18}$$

where the variables are given in figure 3.5. Solutions to these equations will only give values of variables when the SHG is most efficient, i.e. the central value of a certain SH bandwidth. The variables here are the pump angle relative to the lattice and the pump wavelength.

4 KTP properties

The choice of nonlinear material will greatly depend on the fabrication method and the desired properties of the engineered structure. A nonlinear photonic crystal can be manufactured by periodically inverting the spontaneous polarization in two dimensions in a ferroelectric crystal, which is the approach that has been used in this thesis work.

A crystal has to fulfill several requirements in order to be suitable for nonlinear optics. First of all, it has to have high intrinsic nonlinearity. The term high is of course a vague quantification. What it means is that it should be possible to generate frequency conversion from a laser source, and the higher the better. Below I will list further important properties for being a candidate.

- Wide transparency range
- Large size with optical and structural homogeneity
- Chemical and mechanical stability
- Low cost and easy fabrication
- High resistance to optical damage

Of course, the crystal has to be transparent in the range of the interacting wavelengths. This is mainly a problem for wavelengths in UV or far-IR range. The available size of the crystal can also be a limitation, depending on application and processing steps. Chemical and mechanical stability mean that the crystal has to stand the light intensities and environmental conditions, without changing its properties.

KTP is a promising candidate because of its high resistance to optical damage, excellent mechanical stability and high nonlinearity. The crystal does not exist naturally and it has to be synthesized. Crystals used in this work were manufactured by the flux grown method. All the necessary components are contained in a molten flux in which KTP crystallizes when the flux is cooled. An advantage of the flux growth method, compared to other methods, is that it can be operated under quite simple conditions which makes it a fast and relatively inexpensive process.

4.1 Crystal structure

Potassium titanyl phosphate belongs to the orthorhombic crystal class, acentric point group *mm2* and the space group $Pna2_1$. The principal axes, x, y and z correspond to the crystallographic directions a, b and c of the crystal, where c is the polar axis which is the direction of spontaneous polarization. The lattice

constants are $a = 12.819$ Å, $b = 6.399$ Å and $c = 10.584$ Å. The crystal structure is composed of chains of TiO_6 octahedra, which are corner-linked by PO_4 tetrehedra, see figure 4.1. The TiO_6 octahedra is slightly distorted, consisting of short and long Ti−O bonds, which build up a helical chain along the c-axis. The K^+ ions are located in these channels, weakly bonded to both the octahedra and tetrahedra. In case of a electric field applied at the polar faces of the crystal, these K^+ ions can move, with low activation energy, along the helical chain, which causes the high ionic conductivity. They can occupy two non-equivalent sites; either eight-fold coordinated (K_1) or nine-fold coordinated (K_2). A net spontaneous polarization along the c-axis is induced due to the arrangement of alternating Ti−O bond-lengths. Domain inversion takes place by shifting the K^+ ions in the c-direction, from the eight-fold coordinated cation to the nine-fold coordinated cation, and vice versa [16]. At the same time the short Ti−O bonds turn into long bonds and vice versa. Domain inversion is discussed in the following sections, from a macroscopic point in the ferroelectricity section and more in detail in the domain inversion section.

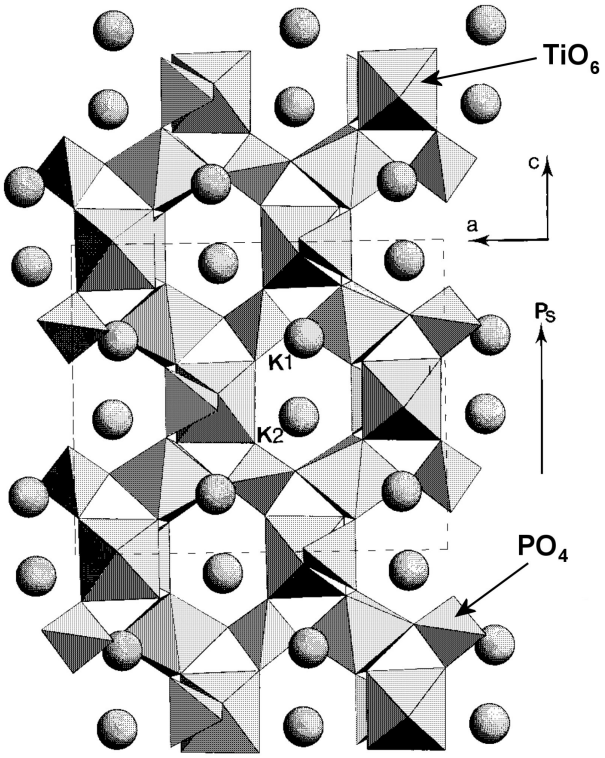

Figure 4.1. *Crystallographic structure of KTP. [17]*

4.2 Ionic conductivity

The conductivity is an important fact to take into account when it comes to domain switching. Higher conductivity will make it more difficult to switch the domains since the energy in the applied field will mainly be wasted to ohmic losses instead of actually switching the domains. KTP has a high ionic conductivity compared to most of the ferroelectric crystals, because of the helical chain structure in the polar direction. The conductivity along the polar axis can be up to four orders of magnitude larger than perpendicular to the polar axis [18]. Due to temperature variations in flux growth process vacancies of K^+ ions are built into the structure, thus increasing conductivity. The conductivity usually varies as a parabolic function along the y-axis, increasing by a factor 2 from the edge to the center [17].

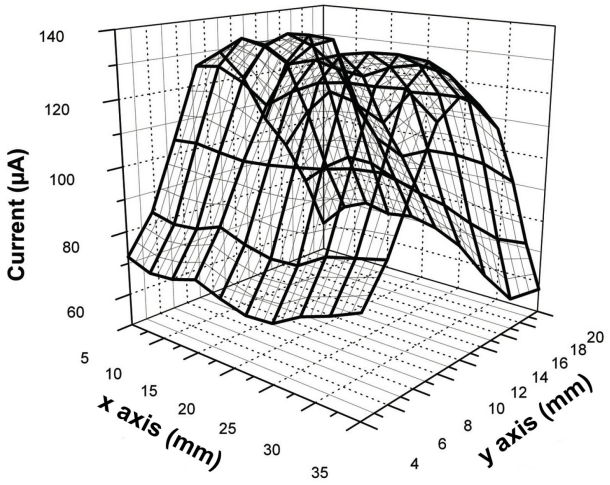

Figure 4.2. *Typical conductivity variation of a flux grown KTP wafer. The 100* µA *level corresponds to a conductivity of* 8.5×10^{-7} S/cm *[17].*

4.3 Ferroelectricity

A ferroelectric crystal is a material with a nonzero spontaneous polarization, due to a non-symmetric arrangement of positive and negative ions. The spontaneous polarization, P_s, is defined as the sum of all the individual dipole moments per unit volume.

A further constraint is that a ferroelectric crystal should have two or more stable equilibrium states in the absence of an electric field and can be shifted from one to another by applying an electric field. Most ferroelectrics undergo a structural phase transition at a temperature known as the Curie temperature, T_c. At this temperature they undergo a transition from a low temperature ferroelectric state to a non-ferroelectric state of higher symmetry, see figure 4.3. The

spontaneous polarization is decreasing with increasing temperature and finally vanishes at the Curie temperature.

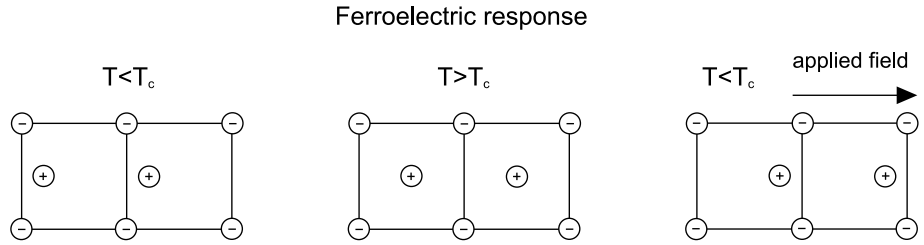

Figure 4.3. *Ferroelectric structural phase transitions.*

4.4 Domain switching

Domain switching of the spontaneous polarization P_s, in an area A, can be achieved by delivering a charge, $Q = 2AP_s$. The electric field that is needed to switch half of the spontaneous polarization in a certain region is defined as the coercive field. A region with a uniform polarization is called a ferroelectric domain. However, the coercive field is not a precise quantity describing domain switching, it only gives an approximate value of the electric field in which to expect domain switching. It is difficult to define since it depends on temperature, measuring frequency and waveform of the applied voltage.

The domain velocity in KTP, defined as the average length of the formed domains divided by the length of the pulse, is different in different crystal directions. The velocity along the b-axis is ~ 30 times larger than in the a-direction and the velocity along the c-axis is at least two orders of magnitude larger than in the ab-plane. [17]. These growth properties are in general beneficial when manufacturing 1D QPM structures, whereas they become a problem for a 2D structure. This has also been seen experimentally where the domain merging is more pronounced along b-axis compared to the a-direction.

4.5 Optical properties

KTP has been extensively used for frequency conversion both in optical parametric oscillators (OPO) and SHG with spectral range from UV to near IR. The transmission window is shown in figure 4.4(a) which extends from 0.365 µm up to around 4.3 µm. The sudden drop in transmission at 2.8 µm is due to the absorption line of OH groups grown into the crystal.

To be able to determine the exact QPM period Λ, it is essential to have accurate values of the index of refraction as a function of wavelength. KTP is a biaxial crystal with different index of refraction for the principal axes of the crystal. Light has been polarized along the z-axis for all measurements conducted

in this thesis. The dispersion relation is usually expressed as a two-pole Sellmeier equation. But in the case of fundamental wavelength < 1 µm it is sufficient to fit a one-pole Sellmeier equation of the form,

$$n_z^2 = A + \frac{B}{1 - \frac{C}{\lambda^2}} + D\lambda^2 \ . \tag{4.1}$$

where λ has to be in µm. Several different fits of this equation to experimental values has been done where the values by Fan *et al.* [19], given in table 4.1, have proved to be accurate for wavelengths below 1 µm, which is the case for wavelengths used in this work ($400 - 950$ nm). A plot of the dispersion for these Sellmeier coefficients for n_z is given in figure 4.4(b).

A $(-)$	B $(-)$	C (μm^2)	D (μm^{-2})
2.25411	1.06543	0.05486	0.02140

Table 4.1. *The Sellmeier coefficients for KTP for $\lambda < 1$ µm, [19].*

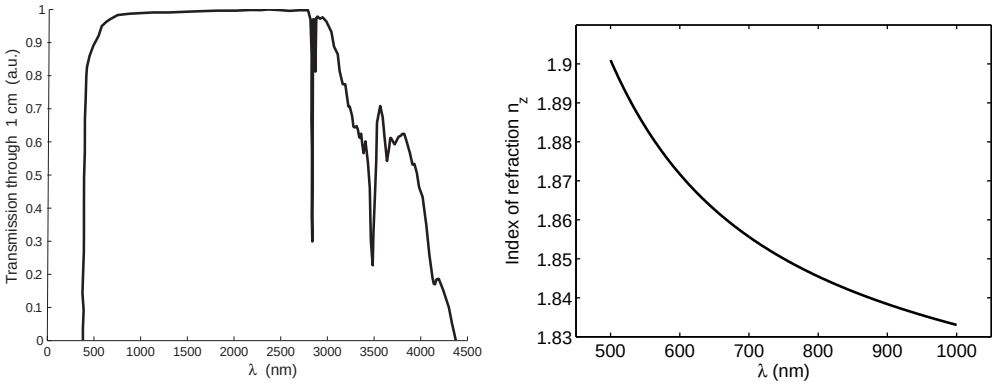

(a) *Transmission window for KTP [20].*

(b) *Dispersion characteristics for KTP (Eq. 4.1)*

Figure 4.4. *Optical properties of KTP.*

The index of refraction is also temperature dependent due to the thermo-optic effect. This is a fortunate property since it gives the possibility to temperature tune phase-matching processes. In order to predict the tuning characteristics it is necessary to have knowledge about the thermal dispersion. This is often described by a Laurent series,

$$\frac{\partial n_z}{\partial T} = \frac{a}{\lambda^3} + \frac{b}{\lambda^2} + \frac{c}{\lambda} + d \ , \tag{4.2}$$

where the z-component of the dependence is considered. The dispersion coefficients have been measured by Wiechmann *et al.* [21] and fit well for wavelengths < 1 µm. The thermal expansion coefficient will also affect the QPM condition due to a change in grating period, but this effect is much smaller than the thermal dispersion.

a (µm^{3}K^{-1})	b (µm^{2}K^{-1})	c (µmK^{-1})	d (K^{-1})	Thermal exp. (K^{-1})
12.415×10^{-6}	-44.414×10^{-6}	59.129×10^{-6}	-12.101×10^{-6}	11×10^{-6}

Table 4.2. *The thermal coefficients for KTP, [21, 22]*

To give a numerical example of the tunability, consider SHG at fundamental wavelength 946 nm. A temperature change, $\Delta T = 80$ deg gives a change in wavelength, $\Delta\lambda \approx 5$ nm for the fundamental beam.

KTP belongs to the orthorhombic crystal class, *mm2*, which will give only 5 nonzero elements in the d-tensor,

$$d = \begin{pmatrix} 0 & 0 & 0 & 0 & d_{15} & 0 \\ 0 & 0 & 0 & d_{24} & 0 & 0 \\ d_{31} & d_{32} & d_{33} & 0 & 0 & 0 \end{pmatrix} . \tag{4.3}$$

The values of these coefficients were measured by Vanherzeele and Bierlein [23] at 1.064 µm and are given in table 4.3.

d_{15} (pmV^{-1})	d_{24} (pmV^{-1})	d_{31} (pmV^{-1})	d_{32} (pmV^{-1})	d_{33} (pmV^{-1})
1.9	3.6	2.5	4.4	16.9

Table 4.3. *The nonlinear coefficients for KTP at 1.064* µm *[23]*

It is evident that d_{33} is the preferred coefficient to use since it is the largest. That corresponds to all interacting fields polarized along z-direction.

4.6 Comparison of nonlinear materials

Lithium niobate $LiNbO_3$ (LN) has been extensively used for 1D QPM during the past 20 years. After Berger suggestion of a nonlinear photonic crystal Broderick *et al.* [24], were the first to report on fabrication of a 2D NPC in LN. To the best of our knowledge, a 2D QPM device has never been realized in any other crystal than lithium niobate and lithium tantalate [25].

KTP has many advantageous properties that makes it an attractive nonlinear material. Besides properties similar to LN it has several very important advantages. Although LN has larger nonlinearity compared to KTP, KTP possesses much lower sensitivity to photorefractive damage and the coercive field is considerably lower. This makes it much easier to fabricate QPM devices that can be used in room temperature. Due to the crystal structure of KTP, domain broadening is limited, at least in one direction, which facilitates the manufacturing process.

5 Poling of two-dimensional structures

It is a challenging task to achieve a uniform 2D QPM structure inside a crystal where every domain has an opposite spontaneous polarization to its neighbors. For the structures designed in this work it means roughly 500 000 inverted domains over an area of 7×3 mm^2. We have manufactured two nonlinear 2D QPM crystals of different periods, by a lithographic patterning process together with electric field poling. Both samples have a rectangular lattice with the same period, 6.09 µm in x-direction but different periods in y-direction, 6.00 µm and 30.00 µm, respectively.

5.1 Processing steps

The as-purchased wafers were cut into smaller pieces, appropriate for the application and to get pieces of homogeneous conductivity. Crystals used in this work were cut to a size of 11×7 mm^2 ($x \times y$) and polished on the x-faces since the light will propagate along the x-axis.

After the cutting and polishing the crystal is prepared for a standard lithographic step conducted in a cleanroom environment. The purpose is to generate a 2D insulating layer with openings that allow for electrical contact to the crystal in the poling step. To begin with, the sample is carefully cleaned in different steps with acetone and deionized water. After that a 2 µm thick layer of positive photoresist (Shipley Microposit S1818) is spun onto the c^--face. Then the sample is pre-baked on a hotplate at 105 deg C for 90 s in order to harden the resist. Now the crystal is ready for illumination in a mask-aligner (Karl-Suss MJB3) using the g-line of a Hg lamp at 436 nm. The mask consists of a aluminum-raster pattern with rectangular openings of 50 % duty-cycle, on top of a glass plate. The mask-aligner is used to align the mask direction of 6.09 µm period parallel to the x-axis of the crystal and illuminate the uncovered area of the photoresist. The size of the patterned area is approximately 8×4 mm^2 ($x \times y$).

Following the illumination, the sample is ready for development, using a developer (Shipley Microposit MF351) diluted with water. Two important parameters that have to be optimized for a successful patterning work are illumination time and development time. As was described in chapter 4.4, the domains will broaden, mainly in y-direction. Therefore it is important to find a duty-cycle of the openings for the photoresist that will give a 50 % duty-cycle for the final, poled, domains. A typical duty-cycle used in this work has been 15 % in both directions for the 6.09×6 µm^2 sample, and in x-direction for the 6.09×30 µm^2 sample, whereas it was considerably larger in y-direction.

The final step before poling is evaporation of a aluminum film (50-100 nm thick). This is done on top of the developed photoresist which means that the aluminum makes contact with the crystal at the openings. Nucleation starts

preferentially in the c^--side and a metal contact enhances the nucleation density [17]. It is only evaporated on the c^--side and not on the opposite side since it is advantageous with nucleation and growing tips from only one side to the other. Hopefully this will limit the domain propagation to one single direction along the z-axis.

5.2 Electric field poling

The basic idea of electric field poling is to deliver a certain amount of charge to the crystal that will periodically switch the spontaneous polarization. There are many variables that can be varied in the poling process and there are by no means a well developed scheme for a successful periodic poling, especially not for 2D QPM in KTP. Therefore we tried to vary three of them; pulse length, pulse amplitude and the number of pulses. The first pulse is always a probe pulse in the low field regime (∼800 V/mm), not to invert the polarization. The purpose is to get a hint about the conductivity of the specific sample before poling. As was mentioned before, edge samples will have a much lower conductivity, which in turn, means lower poling voltage. The probe pulse together with the sample's original position on the wafer will give information about suitable poling settings.

5.2.1 Poling circuit

A signal generator (Agilent model 33120A) was used to give a pulse of chosen amplitude and length which is amplified to the kV range by a high voltage amplifier (Trek model 20/20C), see figure 5.1. Pulse lengths from 500 µs to 6 ms has been used in this work. The voltage across the sample and the current are monitored through the voltage drops, U_1 and U_2 across the resistance R_3 and R_4, respectively. The voltage divider consists of a large resistance R_2 (100 MΩ) to make the voltage measurement passive while the value of R_3 (100 kΩ) is chosen to give a suitable voltage for the oscilloscope. Similarly R_4 (10 kΩ) is chosen to give a suitable voltage for the current measurement. The voltages were measured by an oscilloscope (Textronix TDS2014).

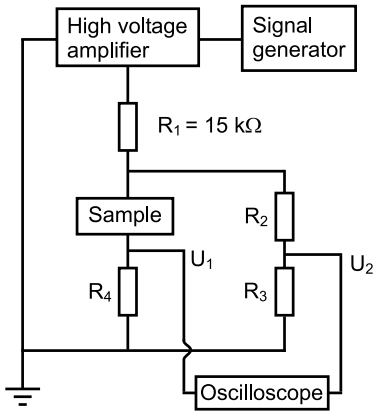

Figure 5.1. *Schematical description of the poling setup. Components and values are explained in the text.*

5.2.2 Periodic domain inversion

The poling voltage can be divided into tow regimes; low field regime, if it is below or close to the coercive field and, high field regime if it is above. It has been observed that the domain inversion will behave differently depending on the poling voltage [17]. Phenomenologically the domain growth, for a 1D QPM structure, can be described in four steps depicted in figure 5.2. First the domain inversion takes place by nucleation of new domains, most pronounced at the edge of the electrode where the electric field is largest (a). After that the tips will grow towards the opposite crystal surface (b). Afterward the domains will broaden horizontally (c), to finally merge under the electrodes (d). In this work we have used a field value very close to the coercive field in order to prevent domain broadening in y-direction.

Electrical contact to the external circuit was provided by a copper electrode. It consists of silicone, wrapped by a thin copper film which provided the contact between the external circuit and the crystal. The non-patterned side of the crystal was coated by electrode gel (Spectra 360 Electrode gel, Parker Laboratories INC.) in order to make a uniform contact between the sample surface and the Cu foil.

5.2.3 Poling settings

Two samples, each of different period, were poled with satisfactory quality with the poling settings given in table 5.4. A probe pulse refers to a pulse that is used to get information about the conductivity while the intention of the poling pulse is to invert the domains in the sample. V_{sample} is the voltage over the sample calculated by measuring U_2. One should note that a higher voltage V_{sample}, for the probe pulse, means lower conductivity of the sample. The progress of the poling was monitored in situ by observation of a non-collinear SHG QPM

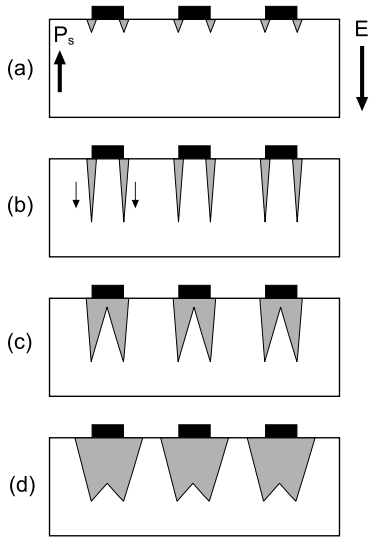

Figure 5.2. *Model describing periodic domain inversion in KTP. (a) Nucleation. (b) Domain propagation. (c) Domain broadening. (d) Domain merging under the electrodes [17].*

peak excited by a cw Ti:Sapphire laser tuned to the appropriate phase-matching wavelength. By moving the sample in z-direction and at the same time observing the intensity it was possible to know how deep the domains had propagated. We terminated the poling when no further increase of the non-collinear SHG intensity was observed. As was mentioned before, the pulse length was also varied. Too few samples have been poled in order to draw some conclusive remarks about optimal pulse length. However, we found out that short pulses (1 ms) limited the domain broadening, mainly in y-direction. Therefore, there is a certain window of process parameters where the poling can be expected to be successful.

In summary, both of the samples have been poled with a relatively low voltage, compared to 1D QPM poling [17], and many pulses. The intention of applying several pulses was to propagate the domains towards the c^+-side, without merging them.

5.3 Evaluation of the poled structure

This section will deal with the results of the optical microscope characterization of the two different NPCs. A easy and fast way to reveal the inverted domain structure on the surface of the crystal is to etch it. The sample is placed in a warm (80 deg C) solution of KNO_3, KOH (2:1 mole ratio) and water for a time typically between 5-15 min. The etchant will attack the c^--surface while the c^+-surface is left essentially untouched, thus revealing the domain structure.

Crystal	pulsetype	V_{sample} (kV)	# pulses	pulse length (ms)
6.09×6	probe	0.84	1	5
	poling	1.92	1	1
		2.1	13	1
6.09×30	probe	0.82	1	5
	poling	2.22	16	1

Table 5.4. *Poling characteristics for the two fabricated samples. The pulse length was 1 ms for all pulses used for these two samples.*

Figure 5.3 shows a typical part of the etched, patterned side of the two samples. The pattern is uniform over the grating area, which manifests the high quality of the manufactured crystal. However, no faithfully reproduced 2D pattern has been observed on the non-patterned side. Figure 5.4 shows an image of the non-patterned side of the 6.09×6 µm^2 sample. It can be clearly seen that the domains have merged in y-direction, for those that have propagated all the way through. The reason for this domain merging can be explained by the different domain growth speeds discussed in section 4.4. However one should remember that this is the first time that a 2D QPM structure has been realized in KTP, hence there are possibilities of optimization of the poling process.

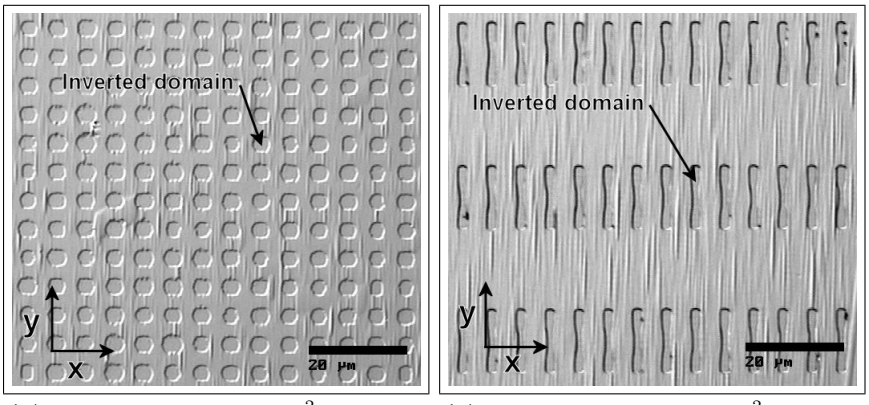

(a) *Micrograph, 6.09×6* µm^2 ***(b)*** *Micrograph, 6.09×30* µm^2

Figure 5.3. *Micrograph images of the etched pattern, former c^--side of the crystals. Characteristic growth striaes can be seen on the non-inverted domains. The scale bar is 20* µm.

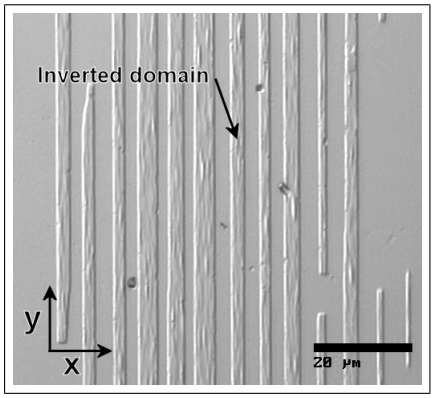

Figure 5.4. *Micrograph image of the etched pattern, former c^+-side of the 6.09×6 µm^2 crystal. Note that domains have merged in y-direction and the structure is no longer a 2D modulation of the nonlinearity. The scale bar is 20 µm.*

Another way to determine the uniformity of the pattern is to analyze the far field diffraction. A 532 nm laser beam was aligned perpendicular to the sample, allowing light to propagate along the z-direction. The selective etching process created a small difference in thickness between the positive and negative domains. Hence, the phase of the light will be periodically modulated and its far field diffraction pattern is proportional to the reciprocal lattice. Figure 5.5(a) represents, a almost square, diffraction pattern for the 6.09×6 µm^2 sample whereas figure 5.5(b) represents a rectangular diffraction pattern which is expected from the 6.09×30 µm^2 sample.

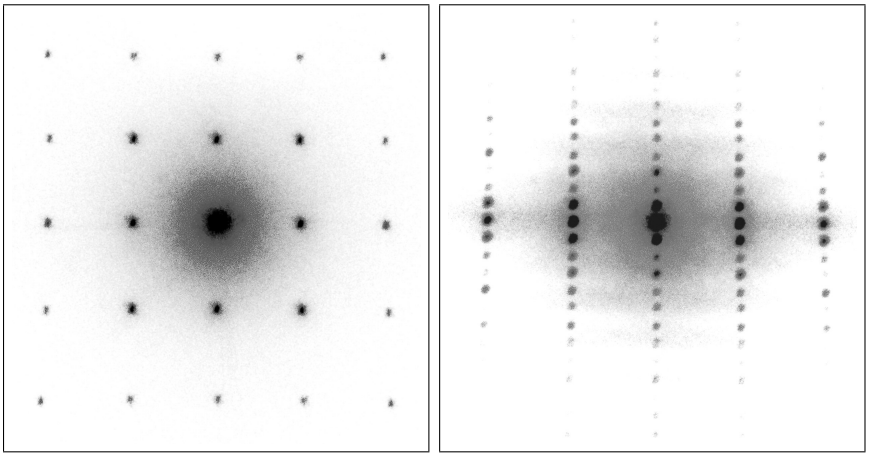

(a) Far-field diffraction, 6.09×6 μm^2 *(b) Far-field diffraction, 6.09×30* μm^2

Figure 5.5. *The etched structure will introduce a modulation of light propagating along the z-axis of the crystal. This far-field diffraction pattern is directly proportional to the reciprocal lattice. The image is a negative, where dark area represents high intensity.*

By scanning the beam over the pattern it was possible to provide information about the homogeneity of the etched structure. However, this method will only give knowledge about the surface structure but not about the switched domains in the bulk. Basically the same information can be retrieved by using an optical microscope, but the diffraction pattern gives a nice demonstration of the reciprocal lattice.

6 Optical characterization

A traditional SHG in a 1D QPM structure is limited to a single wavelength with a narrow acceptance bandwidth. Tuning can be achieved in a narrow interval by either rotating the crystal or changing the phase-matching temperature. To circumvent these limitations and to support several different phase-matching processes in one crystal, a 2D QPM structure is introduced.

6.1 Narrowband pumping

The narrowband pumping enables studies of all accessible phase-matching conditions with a tunable laser, or a specific process with a fixed wavelength laser. A narrowband source in this context refers to a bandwidth < 0.5 nm. The lasers that were used were a continuous wave (cw) Ti:Sapphire laser and a pulsed Nd:YAG laser (946 nm).

6.1.1 Wavelength tuning

In this section the results of SHG of a cw laser source will be presented. We demonstrate a NPC that can support SHG in a discrete set of wavelengths from a Ti:Sapphire laser. To the best of our knowledge, this is the first time SHG is demonstrated in a NPC from a cw laser. Not only the fact that SH light can be generated is important, but also the powers of that light. Therefore, we also measure the power of the generated light. As can be seen from Eq. (2.17) the intensity of SH light is proportional to the square of the fundamental light. Therefore, it is customary to define a normalized conversion efficiency in order to be able to compare different materials and experimental conditions,

$$\eta_{norm} = \frac{P_{2\omega}}{P_{\omega}^2 L} \ . \tag{6.1}$$

L is the length of the crystal and $P_{2\omega}$ and P_{ω} are the powers of the SH and fundamental beams, respectively. On should remember that this is a simplified expression for the intensity (originating from plane wave analysis resulting in Eq. (2.17)), that does not take a gaussian beam shape into account. The full analysis of gaussian focusing conditions is govern by an extensive work developed by Boyd and Kleinman [26].

A CW Ti:Sapphire laser (Spectra Physics Model 3900S pumped by 10 W Milennia X_s) was used for all of the temperature tuning measurements. A half wave plate ($\lambda/2$) was used to rotate the polarization 90 deg to a z-polarized state appropriate for the d_{33} coefficient. Following the half wave plate, a linear polarizer (LP) was used to control the intensity of the light. A convex lens (L) $f = 300$ mm was used to focus the light to a beam waist of $w_0 = 50$ µm ($1/e^2$

intensity). A screen, perpendicular to the fundamental beam, was used to observe the phase-matching angles. Figure 6.1 demonstrates the necessary parts in this simple setup for SHG.

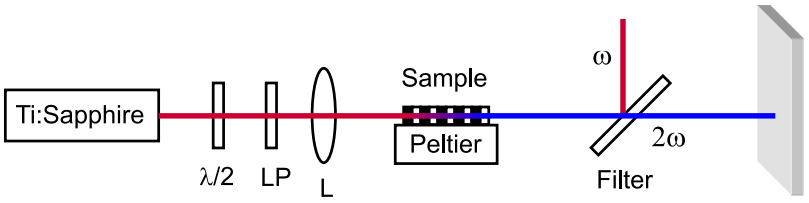

Figure 6.1. *Schematical description of the setup used for wavelength tuning measurements. The different parts are explained in the text.*

The fundamental wavelength was swept over a range, $850 - 950$ nm, where SHG was observed. For every peak, the wavelength was measured by a spectrum analyzer (HP 86140 A), and the output angle was recorded on the screen. The result is presented in figure 6.2 and agrees very well with the theoretical values. The theoretical calculation is directly based on a numerical solution of the Ewald construction in chapter 3.3.3 together with the Sellmeier equation. The intensity was measured with a power meter for the most efficient directions (i.e. collinear and non-collinear of low order) as well as the intensity of the fundamental beam. The calculated conversion efficiency is presented in table 6.5 for both of the samples and for the four lowest order of phase-matching directions.

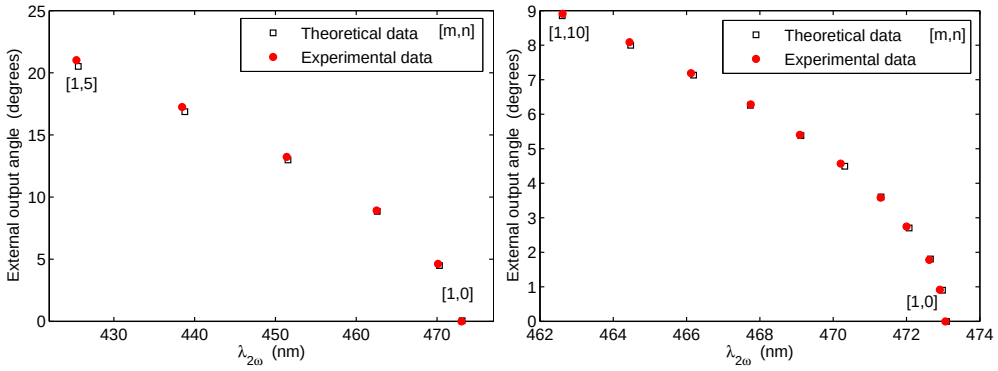

(a) *Sample 6.09×6* μm^2 ***(b)*** *Sample 6.09×30* μm^2

Figure 6.2. *Graph of the experimental (circles) and theoretical (squares) output angles for the SH light as a function of wavelength. The angles are measured in air and relative to the fundamental input beam where 0 degrees indicates collinear propagation. The values in parentheses are the indices specifying the RLV* G_{mn} *involved in the phase matching.*

Crystal	RLV [m,n]	η_{norm} (%/(Wcm))
6.09×6	[1,0]	0.06
	[1,1]	0.006
	[1,2]	0.0002
	[1,3]	0.0004
6.09×30	[1,0]	0.07
	[1,1]	0.002
	[1,2]	0.0002
	[1,3]	0.0014

Table 6.5. *Result of the efficiency measurements in terms of normalized conversion efficiency for different RLVs.*

It can be seen that the efficiency is substantially lower for non-collinear interaction compared to collinear. The reason is a combination of both a reduced interaction length and a smaller Fourier coefficient G_{mn}, discussed in chapter 3.3.2.

However, the focusing conditions used in this experiment are not optimal for maximum conversion efficiency, since the Boyd-Kleinman focusing analysis has not been considered. In another experiment with a cw Ti:Sapphire laser the light was focused by a $f = 50$ mm lens to a spot size of $w_0 = 8$ µm ($1/e^2$ intensity). The maximum normalized conversion efficiency reached 1.5 %/(Wcm) for the 6.09×6 µm^2 sample, in collinear propagation. In our case, a relatively large focus was chosen to aviod beam divergence and the possibility of extra, unexpected, phase-matching conditions.

6.1.2 Angular rotation

In this section we demonstrate all the accessible phase-matching directions limited by the aperture of the crystal. This measurement will give information about which Fourier orders that are available. It is done in a way very similar to X-ray diffraction in crystallography. In solid state physics the method is referred to as the rotating crystal method where the crystal is illuminated under monochromatic X-ray radiation. Here, the monochromatic source is a pulsed Nd:YAG laser and the sample is rotated around the polar axis (z-axis), see figure 6.3. The laser is a passively Q-switched 946 nm Nd:YAG pumped by a fiber-coupled 808 nm diode, for more information see [27]. Under the conditions used in this setup the pulse repetition rate was 25 kHz with a pulse length of 13 ns. A convex lens (L_1) $f = 100$ mm was used to focus the light to a beam waist of $w_0 = 35$ µm ($1/e^2$ intensity). This corresponds to a maximum peak intensity of 50 MW/cm^2. It

was possible to adjust the intensity by the linear polarizer (LP) and the half wave plate ($\lambda/2$). The sample was mounted on a rotational stage and kept at a stable temperature by a peltier element. Since the laser is not tunable, the temperature tuning of the crystal was employed and phase matching was achieved at 26 deg C.

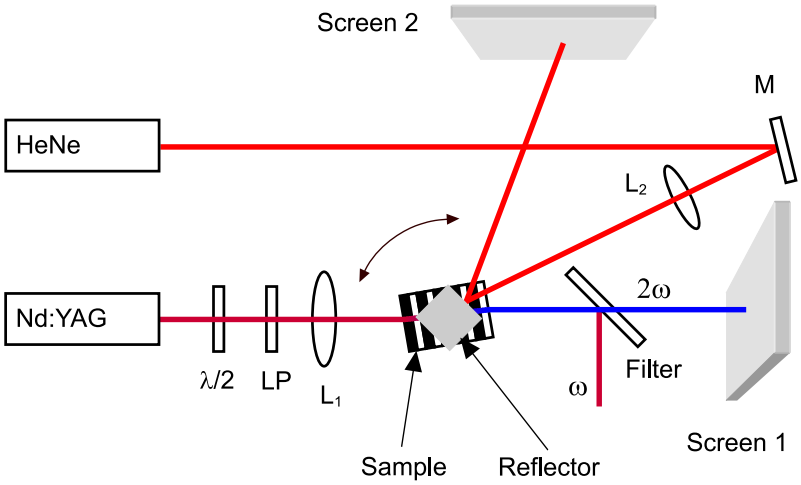

Figure 6.3. *Schematical description of the setup used for the angular rotation measurement. The different parts are explained in the text.*

Next we measured the angular dependence of external output angle as a function of external input angle. The output angle of the SH beam is measured relative to the fundamental beam and is directly observed on screen 1. A flat mirror on the screen was used to align it perpendicular to the fundamental beam. The input angle is defined as the angle between the fundamental beam and the length axis of the crystal (x-axis). Since the angular resolution scale of the rotational stage was not precise enough we used a HeNe laser as an angular probe beam. It was focused by a lens of long focal length (L_2, $f = 300$ mm) to get a narrow spot size on both the reflector and on screen 2. The reflector consisted of a piece of polished glass, which gave a specular reflection. An angle was observed on screen 2 which is related to the external input angle through some simple geometry. When the sample was rotated, sharp SH peaks of varying intensity appeared on screen 1. The position of each peak was noted on both screens which gave the external input and output angles. Both of the samples were characterized in this way and the experimental result is presented as circles in figure 6.4. The theoretical data is numerically calculated by solving the Ewald construction, which in the angular rotation case, is reduced to two coupled equations, Eq. (3.18). There is a good overall agreement between the theoretical and experimental results even for higher order Fourier coefficients which indicates the high quality of the crystals. The inversion symmetry of the angular relation is expected since the rectangular

lattice exhibits inversion symmetry.

The conversion efficiency will reach much higher values for a pulsed system compared to cw, since the peak energy is considerably higher. In this case, the pump depletion has to be taken into account and the second-harmonic conversion efficiency is given by [18],

$$\eta = \frac{\overline{P}_{2\omega}}{\overline{P}_{\omega}} \ . \tag{6.2}$$

The SHG power was measured for collinear propagation for both samples and first non-collinear for the 6.09×6 µm^2. It was not possible to access other orders of phase-matching since the laser wavelength was fixed and the phase-matching wavelength could just be slightly tuned by changing the temperature of the crystal.

Crystal	RLV [m,n]	η (%)
6.09×6	[1,0]	32
	[1,1]	8
6.09×30	[1,0]	29

Table 6.6. *Results of the efficiency measurements in terms of conversion efficiency for pulsed light and different RLVs.*

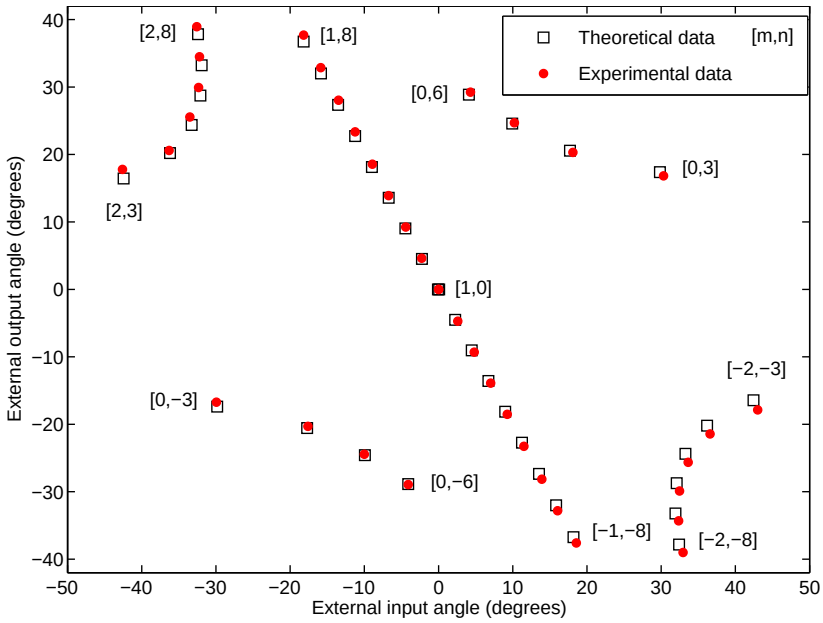

(a) *Sample 6.09×6* μm^2

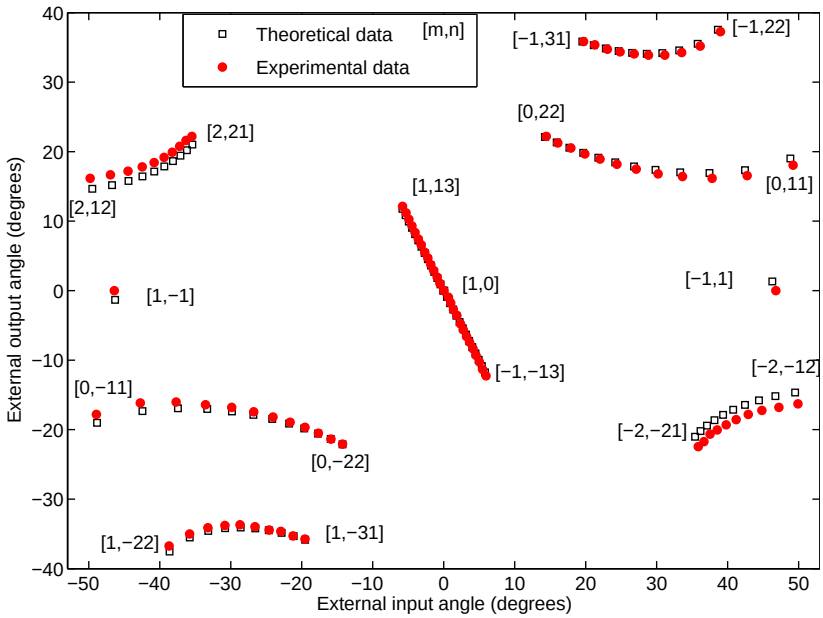

(b) *Sample 6.09×30* μm^2

Figure 6.4. *Graph of the experimental (circles) and theoretical (squares) output angles for the SH light as a function of input angle. The angles are measured in air and relative to the fundamental input beam and 0 degrees indicate collinear propagation. The values in parentheses are the indices specifying the RLV* G_{mn} *involved in the phase matching.*

6.2 Bandwidth issues

It is interesting to investigate the bandwidth issues for the 2D QPM scheme, from a fundamental point of view. A 1D QPM crystal has a narrow acceptance bandwidth, which makes it impossible to generate broadband SH. Different alternative concepts has been suggested in the 1D QPM case, such as quasicrystals and chirped gratings (i.e. the period increases linearly with distance). The acceptance bandwidth is also an important parameter since it gives a upper value, from a efficiency point of view, for the bandwidth of the fundamental laser source. As it will be explained, temperature and wavelength tuning in collinear propagation can also give information about the quality of the QPM structure.

6.2.1 Thermal bandwidth

The thermal bandwidth is measured by sweeping the temperature while measuring the intensity. When the temperature is tuned, two processes will contribute to the phasemismatch. Firstly, the thermal dispersion of the refractive indices will cause a change in Δk and secondly, the thermal expansion will alter both the period Λ and the total length of the structure L. Following Fejer *et al.* [13] a first order expansion in Δk will give the following expression for the full width at half maximum (FWHM) thermal bandwidth for the SHG light,

$$\Delta T_{\mathrm{FWHM}} = \frac{0.4429\lambda_\omega}{L}\left|\frac{\partial}{\partial T}(\Delta n) + \alpha\Delta n\right|^{-1}, \tag{6.3}$$

where α is the thermal expansion coefficient in x-direction and $\Delta n = n_{2\omega} - n_\omega$ is the difference in index of refraction. The derivative is given by Eq. (4.2) evaluated at the wavelengths $\lambda_{2\omega}$ and λ_ω, respectively. The change of Δk implies that the intensity should have a sinc^2 dependence on temperature, which it indeed had. L is the length of the structure containing uniform periods. This bandwidth expression is based on a analysis of a 1D QPM structure, but it should be valid for a 2D QPM in the case of collinear propagation.

A CW Ti:Sapphire laser (Spectra Physics Model 3900S pumped by 10 W Milennia $\mathrm{X_s}$) was used for all of the bandwidth measurements. The fundamental beam was polarized in z-direction by a half wave plate ($\lambda/2$) and a linear polarizer (LP). The beam was focused by a $f = 200$ mm lens ($\mathrm{L_1}$) to a beam waist of $w_0 = 30$ µm ($1/e^2$ intensity) into the crystal. The fundamental power of 550 mW correspond to a intensity of 19 kW/cm^2 in the focus. An imaging system was used to image the spot of SH light at the facet of the crystal onto a photodiode (PD) (Thorlabs DET-200). This setup was chosen to get accurate measurements since the external output angle of the SH beam will change with temperature and thereby the position of the spot at the photodiode, if only one focusing lens is used. As a numerical example, the external output angle for the RLV G_{11} peak is increasing with 1.3 degrees when the temperature is increased 70 deg C, for the 6.09×6 µm^2 sample. By using the one to one imaging system consisting of

the lenses L_2 (f = 100 mm) and L_3 (f = 100 mm) the angular variation will be minimized and hence the spot will be steady at the center of the photodiode. Measurement values of the intensity were taken by an oscilloscope (Textronix TDS 5104) together with a chopper (Stanford Research System SR 540). The chopper was used in order to minimize detection of stray light from the surrounding, rotating at a frequency of 75 Hz, not to coincide with multiples of 50 Hz power line interference. A peltier element was used together with a temperature controller (ILX Lightwave LDT-5525) of PID-type in order to achieve the temperature tuning. Figure 6.5 illustrates the experimental setup.

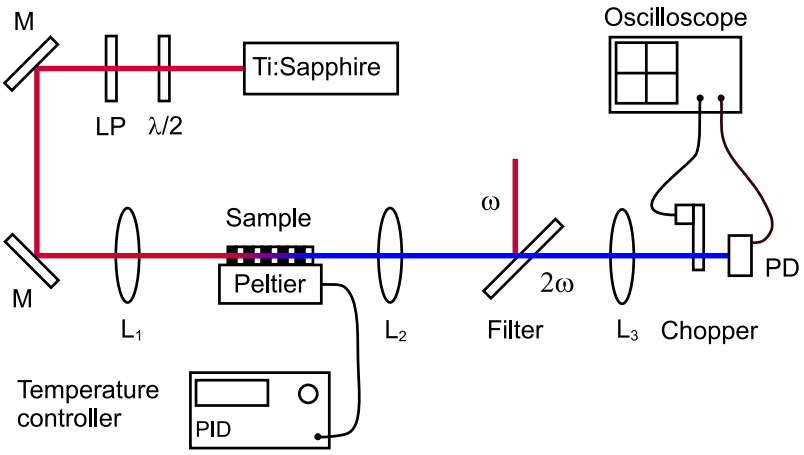

Figure 6.5. *Schematical sketch of the setup used for temperature tuning measurements. The different parts are explained in the text.*

The result of the temperature tuning in collinear direction is presented in figure 6.6.

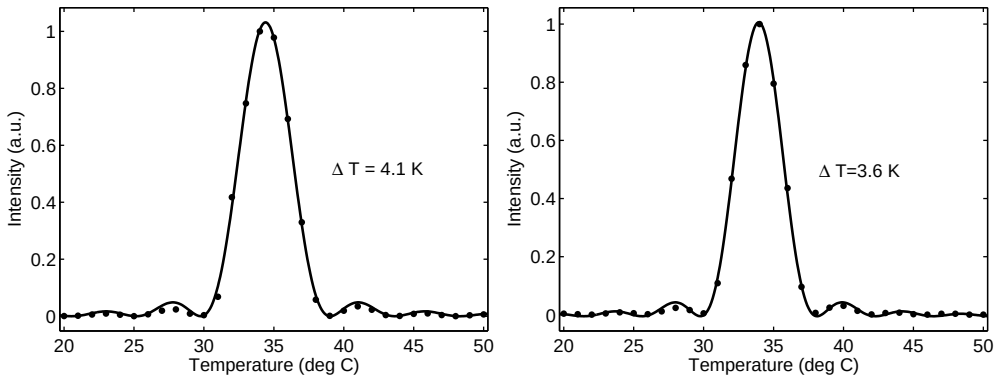

(a) *Sample 6.09×6* μm^2 *SHG at 473.32 nm* ***(b)*** *Sample 6.09×30* μm^2 *SHG at 473.32*

Figure 6.6. *SH intensity around 473* nm *as a function of temperature. Measured for collinear propagation, RLV* G_{10}*. The solid line is a* sinc^2 *fit.*

The intensity dependence follows the expected sinc^2 behaviour. It is customary to calculate an effective length L_{eff} from Eq. (6.3) by solving for L and plug in the measured thermal bandwidth. A specific crystal is poled with expected good quality if the effective length is comparable with the physical one. This was calculated for both of the samples along the RLV G_{10} and the values are given in table 6.7.

Crystal	ΔT (K)	L (mm)	L_{eff} (mm)
6.09×6	4.1	7.0	6.0
6.09×30	3.6	8.5	6.8

Table 6.7. *Result of the thermal bandwidth measurement in collinear propagation and a comparison between the calculated effective length,* L_{eff} *with the measured grating length,* L*.*

What is of more importance is to characterize the tuning properties for non-collinear propagation. The temperature bandwidths are presented in figure 6.7 for light propagating along the RLV G_{11}.

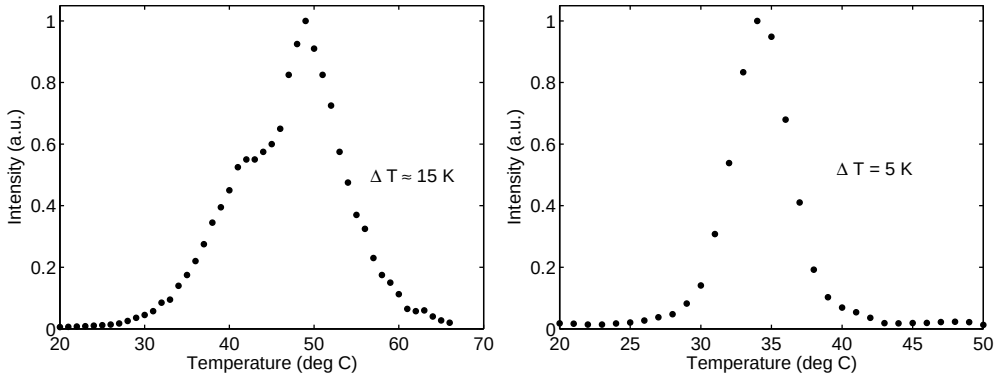

(a) *Sample 6.09×6* µm^2*, SHG at 470.87* nm. ***(b)*** *Sample 6.09×30* µm^2*, SHG at 473.24* nm.

Figure 6.7. *SH intensity as a function of temperature. Measured for first non-collinear propagation, RLV G_{11}.*

The striking result is that the bandwidth is about three times larger for the 6.09×6 µm^2 sample compared to the 6.09×30 µm^2 sample and both of the samples exhibit a broadening compared to collinear propagation. This increase in bandwidth has also been seen by Broderick [24], in the case of non-collinear propagation in a hexagonally poled LN crystal. Temperature tuning is equivalent to wavelength tuning of the pump and hence it should be possible to obtain efficient phase match over a wider wavelength range for non-collinear propagation.

6.2.2 Spectral bandwidth

Similarly to the temperature tuning one can also analyze the spectral tuning. It is motivated since it gives a possibility to compare it to the temperature tuning. For a uniform grating of length L, the wavelength acceptance bandwidth for the fundamental beam is given by [13],

$$\Delta\lambda_{\omega\mathrm{FWHM}} = \frac{0.4429\lambda_\omega}{L}\left|\frac{n_{2\omega}-n_\omega}{\lambda_\omega}+\frac{\partial n_\omega}{\partial\lambda}-\frac{1}{2}\frac{\partial n_{2\omega}}{\partial\lambda}\right|^{-1}. \tag{6.4}$$

From a experimental point of view, the bandwidth can be measured in two different ways. Either one has a tunable narrowband laser and sweeps the wavelength while measuring the intensity, or one uses a broadband laser covering the expected bandwidth. The former option was chosen here, with the same setup as described in the thermal bandwidth section. Differently from the temperature tuning, the wavelength was tuned while the temperature was kept constant. The wavelength of the fundamental beam was recorded by a spectrum analyzer (HP

86140 A). A narrowband excitation was achieved, since the bandwidth of the laser was smaller 0.07 nm, which was the resolution of the spectrum analyzer. This bandwidth is smaller than the bandwidth of the measured spectrums, which ensures narrowband excitation.

The spectrums were recorded by tuning the wavelength and measuring the corresponding power. Measurement values are not taken at evenly spaced points since the wavelength of the laser was not continuously tunable. At some wavelengths it made a jump of 0.1 nm, probably due to longitudinal cavity modes in the laser. However, this was not a severe problem since the main feature of the spectrums were attained. Spectrums for collinear propagation is given in figure 6.8 and non-collinear in figure 6.9

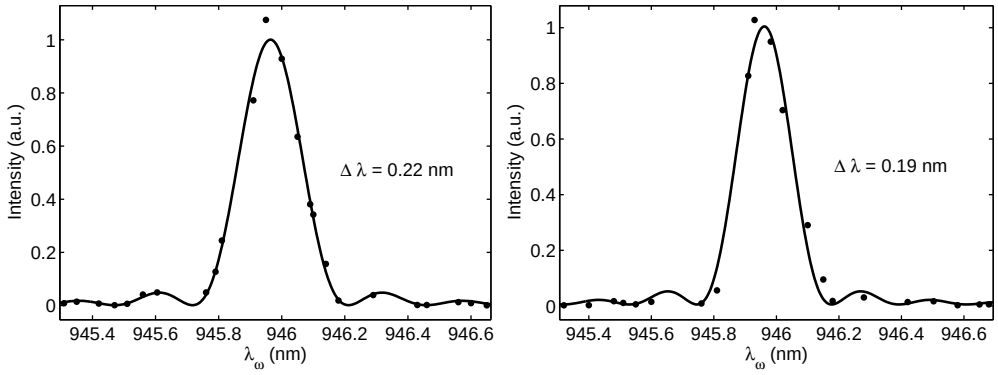

(a) *Sample 6.09×6* µm^2 **(b)** *Sample 6.09×30* µm^2

Figure 6.8. *SH intensity as a function of fundamental wavelength. Measured for collinear propagation, RLV G_{10}. The solid line is a* sinc^2 *fit.*

Similarly to the thermal bandwidth measurement, an effective crystal length was calculated using Eq. (6.4) together with the temperature derivatives, Eq. (4.2). Again, there is an overall agreement in the calculated effective length and the physical length, indicating a high quality of the poled structure.

Crystal	$\Delta\lambda_\omega$ (nm)	L (mm)	L_{eff} (mm)
6.09×6	0.22	7.0	6.7
6.09×30	0.10	8.5	7.7

Table 6.8. *Result of spectral bandwidth measurement in collinear propagation and a comparison between the calculated effective length, L_{eff} with the measured grating length, L.*

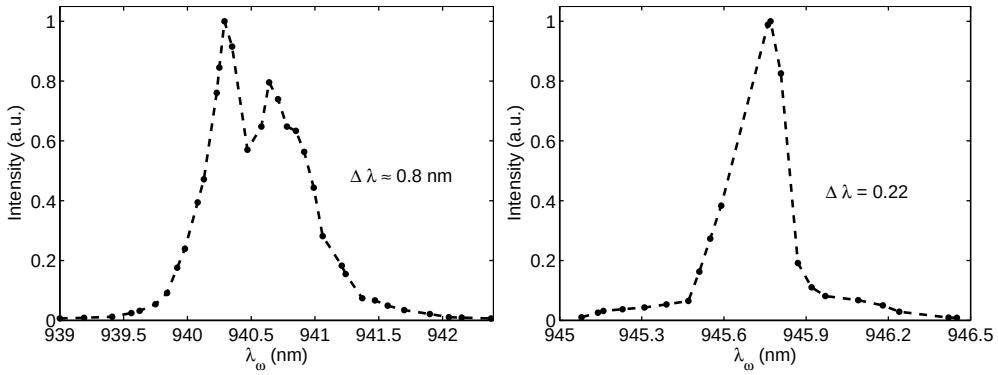

(a) Sample 6.09×6 µm^2 *(b) Sample 6.09×30* µm^2

Figure 6.9. *SH intensity as a function of fundamental wavelength. Measured for first non-collinear propagation, RLV G_{11}.*

6.2.3 Comparison

The two different bandwidth measurements should agree with each other since it is the same physical process going on. Both a change in temperature and wavelength will yield a change in Δk, thus introducing a phasemismatch. In conclusion we observe a 3 times increase in bandwidth for the first non-collinear propagation direction, G_{11} for the 6.09×6 µm^2 sample. Contrary, the increase in bandwidth for the 6.09×30 µm^2 sample is almost negligible. An explanation could be that the walk-off angle θ (see section 3.3.2) for the G_{11} peak is much larger for the 6.09×6 µm^2 lattice, thus increasing the acceptance bandwidth. It is an important feature since it enables the possibility to generate SH light with a broader bandwidth.

6.3 Broadband pumping

In this section we will demonstrate the versatility of a nonlinear photonic crystal in a SHG process. The purpose of using a broadband pump ($\Delta\lambda \approx 10$ nm) is to access several QPM interactions simultaneously, and thus have a multiline coherent light source. A tunable and broadband pump source can be easily achieved by an optical parametric oscillator (OPO).

6.3.1 OPO pump

The broadband laser source was based on a pulsed, tunable OPO, which is essentially a second-order nonlinear process, phasematched in a 1D QPM KTP (PPKTP) crystal, resonated by mirrors. The setup is described in figure 6.10. A pulsed Nd:YAG laser (New wave research's Minilase I/20 Hz) with a repetition rate of 20 Hz and pulse width of 3 ns was used as pump source. The OPO will resonate two interacting beams, the signal and idler, at different wavelengths. These will exit the PPKTP crystal at different angles due to phase-matching conditions. Therefore it is possible to block the idler by an aperture and filter out the remaining pump at 532 nm and let the signal through. Tuning of the wavelength can be achieved by either rotating the crystal or changing the phase-matching temperature. The latter option was chosen in this work with a center wavelength around 941 nm and a bandwidth of 9 nm. The signal was focused to spot size of $w_0 = 700$ µm ($1/e^2$ intensity) by a positive lens with focal length $f = 200$ mm.

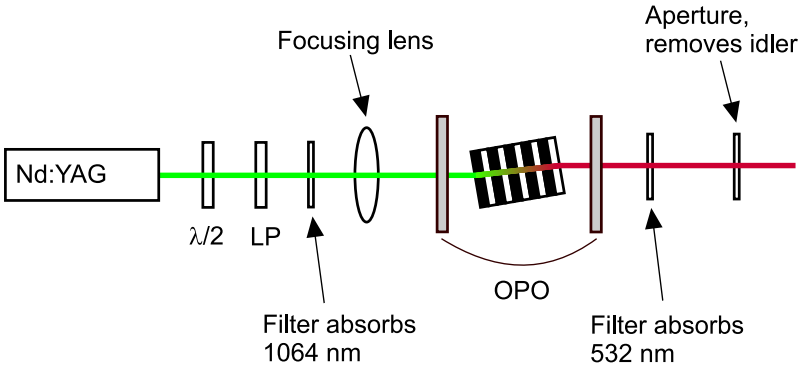

Figure 6.10. *Experimental setup of the broadband OPO laser source.*

The results can be divided into two parts, where the first confirms previous narrowband pumping results, but here with the fundamental light from a broadband OPO, and the second focuses on a multiline tunable coherent source.

In this first part of the measurements, the OPO was adjusted for a center wavelength at 941 nm and a bandwidth of 9 nm, with the spectrum depicted in

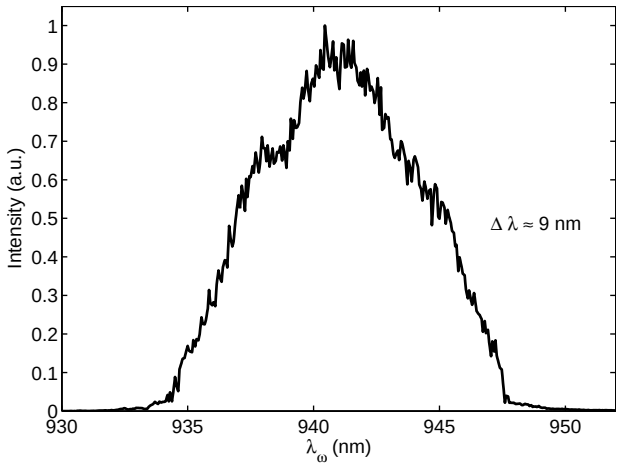

Figure 6.11. *Spectrum of the broadband OPO centered around 941 nm.*

figure 6.11. The output fan of SH light is depicted in figure 6.12 consisting of a collinear beam with RLV $n = 0$ index followed by consecutive higher orders. The angles and wavelengths are given in figure 6.13(a) and are in good agreement with the cw wavelength tuning, figure 6.2(b).

Light from all peaks in the output fan was focused into a fiber and its spectrum was recorded. This combined spectrum, given in figure 6.13(b), contains all peaks up to the fifth order. It is consistent with the cw wavelength tuning as well as figure 6.13(a). Each peaks spectrum was also measured, individually, in order to confirm the correctness of the combined spectrum. An important feature of this combined spectrum is that it contains several lines, relatively closely spaced. It can be described as a discrete broadband generation of SH light, in different directions.

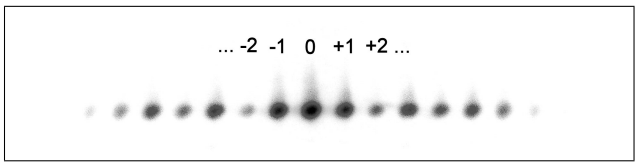

Figure 6.12. *Camera image of the whole output fan with output peaks labeled with its respective RLV n-index. The image is a negative, where dark area represents high intensity.*

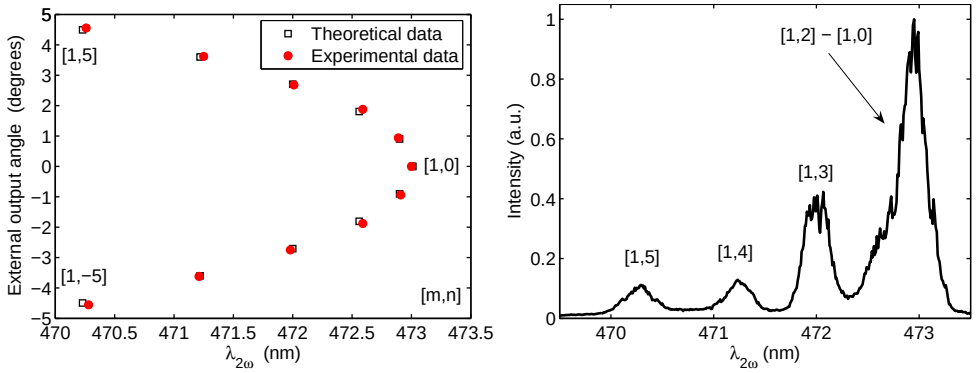

(a) *Output angle as a function of wavelength.* ***(b)*** *Spectrum of the the whole output fan with indicated RLVs.*

Figure 6.13. *Characteristics of the 6.09×30* μm^2 *sample in a broadband OPO setup.*

6.3.2 Tunable multiline coherent light sources

The two different samples were used in a broadband pump setup in order to explore possible multiline generation. A common feature is that the intensity can be interchanged between the generated waves by rotation of the crystal. Also the wavelength of each peak is changed upon rotation, also a common property of QPM. These devices act as a tunable multiline coherent light sources in the blue spectral region.

6.3.2.1 6.09×6 μm^2 sample Three narrowband beams (bandwidth ∼0.2 nm) are generated simultaneously from this setup. The $n = 0$ beam is collinear with the pump and $n = \pm 1$ beams are generated symmetric with a angle separation of 9 deg (full angle). A fundamental beam, from the OPO described above, with center wavelength 941 nm and a bandwidth of 9 nm was used as pump source. The average power of the pump was 12 mW. By rotating the crystal around the polar axis is was possible to tune the wavelength of the two non-collinear beams, see figure 6.14. The optical power for each peak is given on the y-axis.

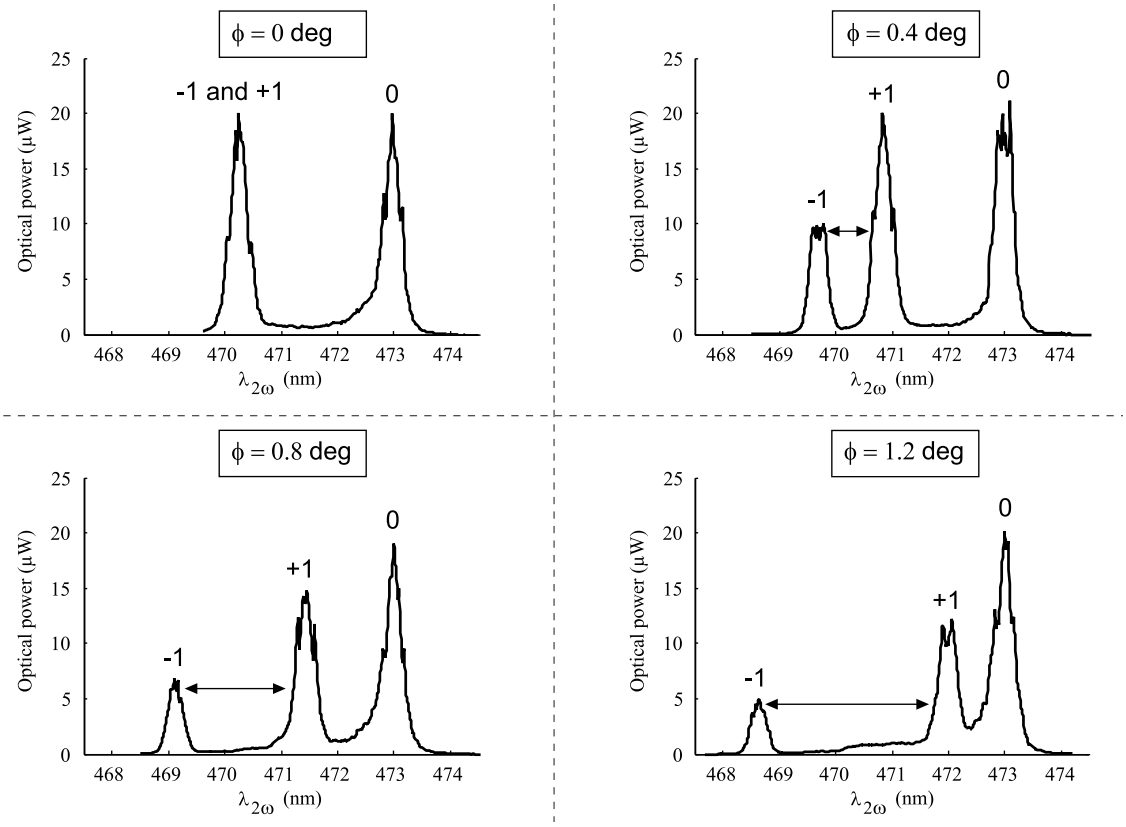

Figure 6.14. *Optical output power from the 6.09×6* μm^2 *sample for different rotational angles of the crystal relative to the fundamental beam. The output peaks are labeled with its respective RLV n-index,* $m = 1$ *for all cases. Note the increasing angular separation between the* $n = \pm 1$ *peaks with increasing angle.*

6.3.2.2 6.09×30 µm² sample Two narrowband beams (bandwidth ∼0.2 nm) originating from the RLV $n = \pm 1$ in figure 6.12 are generated simultaneously with an output angle separation of 1.9 degrees (full angle). All beams according to the output fan, figure 6.12, were present, but only the $n = \pm 1$ were characterized. However, they are assumed to follow a similar behavior as the $n = \pm 1$ beams. A fundamental beam, from the OPO described above, with center wavelength 946 nm and a bandwidth of 10 nm was used as pump source. The average power of the pump was 12 mW. The wavelength separation between the two beams can be chosen in the interval $0 - 4.5$ nm. See figure 6.15 for a graphical illustration of the tuning behavior for 5 different angles as well as the optical output power of each beam. Tuning is achieved by rotating the crystal around the polar axis in the interval 0-9 degrees.

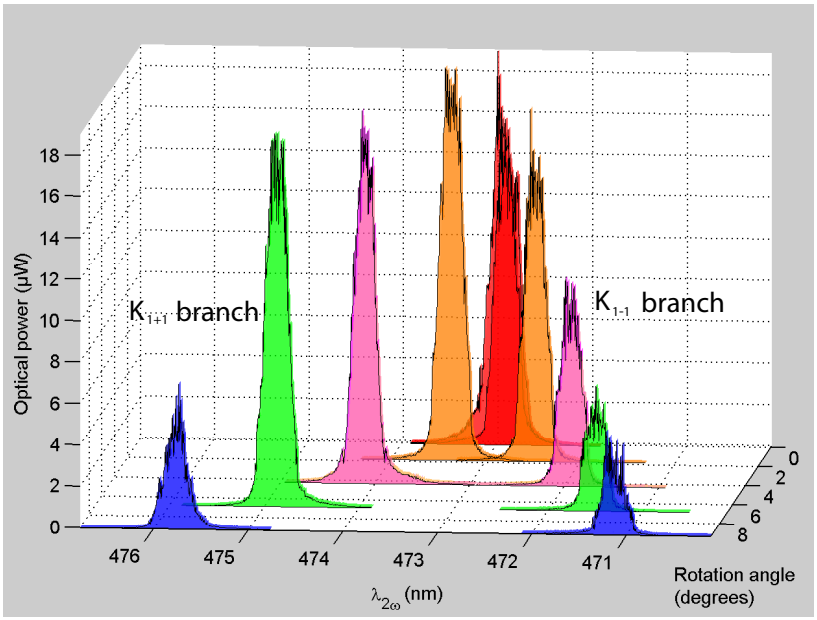

Figure 6.15. *Experimental demonstration of a pulsed two-line coherent light source where the separation can be tuned by rotating the crystal (6.09×30 µm²). The average optical output power for each spectrum is indicated on the z-axis.*

The center wavelength of the SH light is predicted to be tunable slightly more than 2 nm by changing the phase-matching temperature in the interval 70 deg C, see figure 6.16. It should also be possible to adjust the center wavelength of the fundamental beam in order to balance the output power to a desired ratio between the two beams.

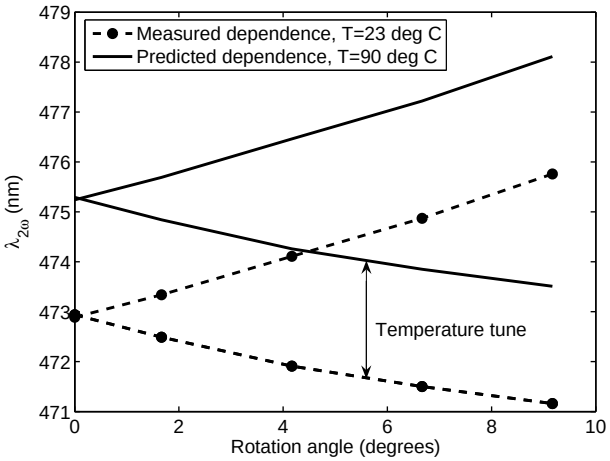

Figure 6.16. *Illustration of the accessible wavelengths by rotation of the 6.09×30* μm^2 *crystal as well as the predicted dependence for higher phase-matching temperature of the 2D QPM.*

7 Conclusions and future perspectives

In this work we have presented a method to manufacture a NPC in KTP, for the first time in this material. To the best of our knowledge, the feature size (periodicity 6.09×6 µm^2) is also the smallest achieved in two dimensions, in a ferroelectric. In conclusion we have manufactured a NPC in KTP, a material much less susceptible to photorefractive damage compared to LN. This device can be used in room temperature and still withstand high intensities. Two crystals of different periodicity has been manufactured, one 6.09×6 µm^2 and the other 6.09×30 µm^2. They can supply phase matching in collinear direction to the pump beam and also several non-collinear directions, all with different wavelengths. Another useful application might be simultaneously discrete SHG, when a broadband pump is used. We also demonstrate a multiline coherent light source, consisting of several beams at different wavelength and whose wavelength separation can be tuned. A increase in bandwidth was also observed for non-collinear propagation. All together, we have characterized and demonstrated phase-matching possibilities in these NPCs by using several different laser pump sources.

7.1 Future work

There are a lot of interesting future work that can be done in the frame of NPCs. Some are more realistic, for example a smart design of the pattern and optimizing the domain propagation, whereas realizing a working all-optical micro-transistor is more difficult and further away in the future.

7.1.1 Optimizing domain propagation

It was evident from the etched structures that it was difficult to propagate cylinder-shaped domains all the way through the crystal. It would be necessary to investigate how deep the domains had propagated by cutting the crystal in slices and etch it. From our measurements, it appeared as the 2D structure gradually merged into a 1D structure along the z-axis.

Apparently, there is a lot of work to do in order to optimize the manufacturing process, and mainly the electric field poling. As was discussed in the fabrication chapter, there is a process window of parameters, where the poling can be successful. In 2D poling this is much smaller compared to 1D poling, since there is an extra dimension in which merging can occur. The goal to strive for is to achieve domain inversion in cylinder shaped fashion along the polar axis, without merging any domains in the xy-plane.

It is not sure that it will be enough to just adjust the poling settings in order to obtain a high quality NPC. Instead it can be feasible to do some pre-poling steps, for example potassium enrichment [17]. The purpose of this chemical

patterning is to periodically increase the potassium concentration, and hence lower the coercive field. The main advantage of this method is that the sample homogeneity is improved and the domain merging is reduced.

7.1.2 Frequency conversion applications

A natural continuation would be to design the pattern of inverted domains, in order to optimize the desired phase-matching conditions. A theoretical work by Lifshitz *et al.* [4] presents a general method for the design of a 2D photonic quasicrystal that can be utilized for simultaneously phase matching of an arbitrary frequency conversion process. A quasicrystal is similar to a usual crystal structure and exhibits symmetry and repeating patterns of unit cells. But, unlike a crystal, this structure requires more than one unit cell to achieve large-order periodicity. In such a quasicrystal, it is possible to have several phase-matching directions and along each direction phase-match different processes. Unfortunately there is an inherent limitation in efficiency of all these non-collinear schemes. The problem resides in the limited interaction length since the spatial overlap between pump wave and generated wave becomes shorter when they propagate in different directions, compared to the collinear case.

Fortunately this problem can be addressed in some cases by implementing a novel design of the phase-matching scheme. This process starts with phase-matched generation of a pair of symmetric second-harmonic waves, which then interact to produce a fourth-harmonic wave that is collinear to the fundamental [28]. Theoretical calculations suggest that this different scheme should be 4 times more efficient compared to a conventional fourth-harmonic 1D QPM process.

7.1.3 Photonic applications

As it was mentioned in the introduction, it would be interesting to combine the guiding properties of a photonic crystal together with a nonlinear material. This could in principle be done in KTP by means of electric field poling and etching. An experiment recently demonstrated 1D periodic poling in KTP with a period of 720 nm, used for SHG [17]. This suggests that it is possible to achieve feature sizes well below one micron. Together with a optimized etching step, it should be possible to produce a photonic structure in a nonlinear material with a hollow cylinder-formed openings.

Another possibility arises when a continuous electric field is applied over such a structure. The opposite domains acquire positive and negative refractive index changes, thus generating a photonic crystal realized in a nonlinear medium. However, the refractive index change is relatively small for voltages that are low enough, to not cause electrical breakdown.

References

[1] M. Yamada, N. Nada, M. Saitoh, and K. Watanabe. First-order quasi-phase matched $LiNbO_3$ waveguide periodically poled by applying an external field for efficient blue second-harmonic generation. *Appl. Phys. Lett.*, **62**:435–6, 1993.

[2] Sergei Mingaleev and Yuri Kivshar. Nonlinear photonic crystals - toward all-optical technologies. *Optics and Photonics News*, **07**:48–51, 2002.

[3] Berger V. Nonlinear photonic crystals. *Physical Review Letters*, **81**:4136 – 39, 1992.

[4] R. Lifshitz, A. Arie, and A. Bahabad. Photonic quasicrystals for nonlinear optical frequency conversion. *Physical Review Letters*, **62**:133901–4, 2005.

[5] M. F. Yanik, S. Fan, M. Soljacic, and J. D. Joannopoulos. All-optical transistor action with bistable switching in a photonic crystal cross-waveguide geometry. *Optics Letters*, **28**:2506 – 8, 2003.

[6] Z. Zalevsky, A. Rudnitsky, and M. Nathan. Nano photonic and ultra fast all-optical processing modules. *Optics Express*, **13**:10272 – 84, 2005.

[7] P.W Milonni & J.H Eberly. *Lasers*. John Wiley, New York, 1988.

[8] John David Jackson. *Classical Electrodynamics*. Academic Press, USA, 3:rd edition, 1976.

[9] Yariv A. *Quantum Electronics, 3rd ed.* John Wiley, New York, 1989.

[10] Richard L. Sutherland. *Handbook of Nonlinear Optics*. Marcel Dekker, Inc., New York, 1996.

[11] P.N Butcher & D. Cotter. *The Elements of Nonlinear Optics*. Cambridge University Press, New York, 1998.

[12] J. A. Armstrong, N. Bloembergen, J. Ducuing, and P. S. Persan. Interactions between light waves in nonlinear dielectric. *Physical Review*, **127**:1918 – 39, 1962.

[13] Martin M. Fejer, G. A. Magel, Dieter H. Jundt, and Robert L. Byer. Quasi-Phase-Matched Second Harmonic Generation: Tuning and Tolerances. *IEEE Journal of Quantum Electronics*, **28**:2631 – 54, 1992.

[14] S. M. Russell, P. E. Powers, M. J. Missey, and K. L. Schepler. Broadband mid-infrared generation with two-dimensional quasi-phase-matched structures. *IEEE Journal of Quantum Electronics*, **37**:877 – 87, 2001.

[15] Neil W. Ashcroft and N. David Mermin. *Solid State Physics*. Brooks Cole, USA, 1:st edition, 1976.

[16] R. Stolzenberger and M. Scripsick. Recent advancements in the periodic poling and characterization of RTA and its isomorphs. *Proceedings of SPIE*, **3620**:23 – 35, 1999.

[17] Carlota Canalias. *Domain engineering in $KTiOPO_4$*. PhD thesis, Department of Physics, Royal Institute of Technology, SE-106 91 Stockholm, Sweden, 2005.

[18] Shunhua Wang. *Fabrication and characterization of periodically-poled KTP and Rb-doped KTP for applications in the visible and UV*. PhD thesis, Department of Physics, Royal Institute of Technology, SE-106 91 Stockholm, Sweden, 2005.

[19] T. Y. Fan, C. E. Huang, B. Q. Hu, R. C. Eckardt, Y. X. Fan, R. L. Byer, and R. S. Feigelson. Second harmonic generation and accurate index of refraction measurements in flux-grown $KTiOPO_4$. *Applied Optics*, **26**:2390 – 94, 1987.

[20] Software package - SNLO. http://www.sandia.gov.

[21] W. Wiechmann, S. Kubota, T. Fukui, and H. Masuda. Refractive-index temperature derivatives of potassium titanyl phosphate. *Optics Letters*, **18**:1208 – 10, 1993.

[22] J. D. Bierlein and H. Vanherzeele. Potassium titanyl phosphate: properties and new applications. *J. Opt. Soc. Am. B, Opt. Phys.*, **6**:622 – 33, 1989.

[23] H. Vanherzeele and J. D. Bierlein. Magnitude of the nonlinear-optical coefficients of $KTiOPO_4$. *Optics Letters*, **17**:982 – 4, 1992.

[24] N. G. R. Broderick, G. W. Ross, H. L. Offerhaus, D. J. Richardson, and D. C. Hanna. Hexagonally poled lithium niobate: a two-dimensional nonlinear photonic crystal. *Physical Review Letters*, **84**:4345 – 8, 2000.

[25] P. Xu, S. H. Ji, S. N. Zhu, X. Q. Yu, J. Sun, H. T. Wang, J .L. He, Y. Y. Zhu, and N. B. Ming. Conical second harmonic generation in a two-dimensional $\chi^{(2)}$ photonic Crystal: a hexagonally poled $LiTaO_3$ Crystal. *Physical Review Letters*, **93**:133904, 2004.

[26] R.W. Boyd. *Nonlinear Optics*. Elsevier Science, USA, 2:nd edition, 2003.

[27] S. Johansson, S. Bjurshagen, C. Canalias, V. Pasiskevicius, F. Laurell, and R. Koch. An all solid-state UV source based on a frequency quadrupled, passively Q-switched 946 nm laser. *Optics Express*, **15**:449 – 58, 2007.

[28] M. De Sterke, S. M. Saltiel, and Y. S. Kivshar. Efficient collinear fourth-harmonic generation by two-channel multistep cascading in a single two-dimensional nonlinear photonic crystal. *Optics Letters*, **26**:539 – 41, 2001.